Master's thesis

NTNU
Norwegian University of Science and Technology
Faculty of Information Technology and Electrical Engineering
Department of Electric Power Engineering

Runar Mellerud

Analysis of Losses and Radial Vibration in a PM Synchronous Machine with Physical Modularity

Master's thesis in Energy and Environmental Engineering
Supervisor: Pål Keim Olsen
Co-supervisor: Robert Nilssen
June 2021

NTNU
Norwegian University of Science and Technology

Runar Mellerud

Analysis of Losses and Radial Vibration in a PM Synchronous Machine with Physical Modularity

Master's thesis in Energy and Environmental Engineering
Supervisor: Pål Keim Olsen
Co-supervisor: Robert Nilssen
June 2021

Norwegian University of Science and Technology
Faculty of Information Technology and Electrical Engineering
Department of Electric Power Engineering

NTNU
Norwegian University of
Science and Technology

Analysis of Losses and Radial Vibration in a PM Synchronous Machine with Physical Modularity

Runar Mellerud
Department of Electric Power Engineering
Norwegian University of Science and Technology
Supervisors: Pål Keim Olsen and Robert Nilssen

***Abstract*— The ModHVDC generator is particularly lucrative for offshore wind power as it reduces the need of several grid components while also improving availability. This solution uses physical modularity, where air gaps divide the stator into separate modules. This could present new challenges concerning altered magnetic performance and loss of rigidity in the structure. The goal of this thesis is to identify losses and radial vibration in a previously designed ModHVDC machine and compare it to its non-modular equivalent. This has been done through finite element modelling in COMSOL.**

Losses in the electrical steel, magnets and copper were estimated. Together these amounted to 259.8 kW at full load in the modular machine, and copper losses was the main contributor with 224.7 kW. Modularity was found to increase steel losses by 22% at full load and 31.5% at no load, while having negligible effect on magnet losses. Magnet segmentation was employed, reducing magnet losses by 96% at full load in the modular machine, from 281 kW to 10 kW.

To evaluate vibration, a harmonic analysis of air gap radial forces was combined with a mechanical analysis. The amplitude of the radial force harmonics were estimated to be close to equal for the modular generator and its non-modular equivalent. Radial vibration was considered unlikely due to 1) the lowest order of the radial force subharmonics was estimated to be 32, 2) the temporal frequency of the force harmonics was 26.67 Hz, far from the module's lowest mechanical eigenfrequency of 322 Hz.

Index Terms*— *Losses, modularity, space harmonics, vibration.

I. INTRODUCTION

Offshore wind offers a sea of opportunities on the road to decarbonization, with vast areas, high winds, high capacity factors and low visual and natural impacts. Its adoption is rapidly increasing, and between 2010 and 2018, the offshore wind market grew by almost 30% per year [1]. According to [2], this trend is expected to continue with an increase in annual offshore wind installations from 6.1 GW in 2020 to 23.9 GW in 2025, which will bring its share to 21% of global new wind installations. To continue this momentum, a further reduction of the levelized cost of energy is needed. The ModHVDC project at NTNU has proposed a generator that could offer reduced capital and operational expenditures along with an increased turbine availability and system efficiency [3]. In this generator, physical modularity allows a series connection of modules, resulting in an output DC voltage of 100 kV or higher that may be transmitted directly to shore.

Physical modularity means that the stator is divided into physically separate modules, introducing air gaps in the stator structure. These will function as flux barriers, restricting the flow of the magnetic flux, which in [4]–[7] were employed to reduce subharmonics. This in turn gave lower losses and an increased machine efficiency. However, none of these machines include an entire base winding in one module as is the case in the ModHVDC design. With regards to losses, this type of structure was only found in [8], [9] where both found that steel losses increase. Air gaps in the yoke will also remove its intrinsic rigidity, and modules could be subject to both large forces and vibrations in the radial and tangential direction. Furthermore, radial forces could also induce vibrations on the stator frame. The consequences of this could be severe stator deformations or support structure deterioration. Previously, vibration of the stator frame has been analyzed for several modular machines in [10].

This thesis will provide an overview over properties and challenges regarding losses and module radial vibration in the modular machine designed in [9]. Further, it may serve as a decision basis for further work in the ModHVDC project and when outlining the cooling and support system. The machine in question is a direct driven permanent magnet synchronous machine with concentrated windings. How modularity influences the results is also investigated through a comparison between the *modular* machine, which has physical modularity, and a *non-modular* equivalent which does not.

This thesis starts with presenting theory of modular generator design and loss estimation before moving on to force harmonics and how they interact with mechanical properties to induce vibration. Then, the methods used for the modelling and analyses are presented. Next follows the results from estimation of magnetic flux, losses, force harmonics, static deformation and eigenfrequencies. A discussion regarding modelling choices, results and their validity is then included before the conclusion of the work is presented along with recommendations for further work.

II. THEORY

This section starts with a brief presentation of modular machine design and how this is applied in the ModHVDC project. Calculation methods regarding losses then follows before theory of vibration estimation is explored through radial force harmonics and mechanical properties.

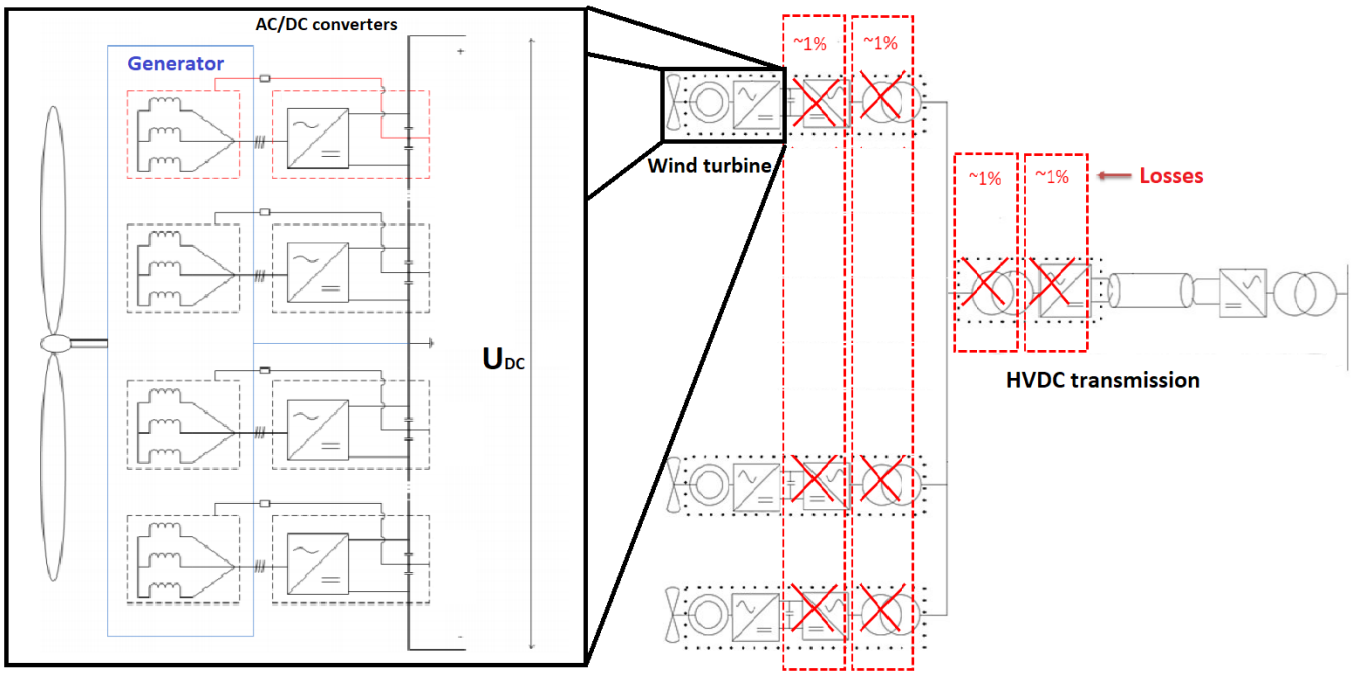

Fig. 1: ModHVDC configuration for offshore wind power.

A. *Modular machine design*

Modularization is the process of decomposing a system into a number of components. In a permanent magnet synchronous machine, two types of modularity are discussed: functional and physical [11].

In an electric machine, the stator windings may be grouped into several modules with their own converter operating independently from each other. This is defined as functional modularity. If a fault occurs in the windings or converter of one or more modules, they may be switched off and bypassed completely. The operation may continue, which results in an improved reliability and availability of the machine.

Physical modularity may be achieved through physical separation of the modules through segmentation of the stator core. This allows replacement of a single module in case of a winding failure. In addition, the smaller parts are lighter and easier to handle, which leads to a quicker and cheaper replacement. The division of the stator structure also presents opportunities to insulate modules from each other both magnetically and electrically. However, it also reduces the rigidity of the stator yoke, which introduces challenges for the support structure.

The converters of each module may either be connected in parallel, series or a combination. A parallel connection has been investigated in [12]–[15] mainly to utilize the high fault tolerance of functional modularity. This solution leads to an equal voltage across all modules, but also a reduced current through the converters. A simplified illustration of this connection for a machine with modules is given in Figure 2.

The series connection was first introduced in [16] and is utilized in the ModHVDC project [17]–[19]. Through

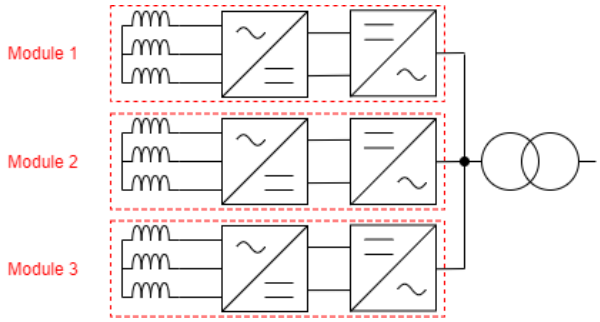

Fig. 2: Parallel connection of modules.

connecting the modules in series as shown in Figure 1, 100 kV or higher DC voltage on the output may be obtained. This can be transmitted through cable directly to shore, reducing the amount of components needed compared to a conventional system, and thus decreasing cost while increasing system efficiency. The module voltage level corresponds to the converter voltage limit, which allows the slot insulation thickness to remain low as the total output voltage increases [17]. Because of the connection structure, the modules operate at different voltages relative to each other. This leads to a requirement of insulation between each module, and such physical modularity is necessary. In the ModHVDC design, functional modularity is achieved through assigning one converter per base winding. This introduces the additional winding rules [9]:

- The phase layout for each module must be symmetrical
- The number of stator slots must be dividable by the number of modules divided by 2

B. Losses

The loss calculation methods need to be different for separate parts of a machine due to different material properties, lamination thickness, magnetic field and current behaviours. Here, they are divided into steel, magnet and copper losses.

1) Steel losses: The CAL2 model in the time domain proposed in [20] was used to calculate the steel losses in the machine. This model was chosen because it was found to have a relative error of only 5% for the 75 kVA, 50 Hz hydro generator investigated in [21]. For the loss modelling described below, losses in watts per kilogram, p, are calculated. To get losses in watts, Equation 1 should be used.

$$P = L\rho N_{sector} \int \int_S p \, dS \tag{1}$$

Here, L is the axial length of the machine, ρ is the steel density, and N_{sector} is the number of sectors corresponding to the whole machine. The loss density is integrated over the surface of one sector.

Losses in the steel of an electric machine may be understood through the concept of loss separation where they are calculated based on the different phenomena occurring in the material. In 1924, Jordan proposed to separate losses into hysteresis and eddy current losses based on their relationship with the frequency, f, and the peak value of the magnetic flux density, $\hat{B}$ [22]:

$$p = K_h \hat{B}^2 f + K_e \hat{B}^2 f^2 \tag{2}$$

Here, K_h and K_e are constant hysteresis and eddy current coefficients respectively. In the original model, the skin effect was neglected, and eddy currents were assumed to be homogeneously distributed, which meant K_e could be calculated analytically through material properties:

$$K_e = \frac{\sigma \pi^2 w_{lam}^2}{6\delta} \tag{3}$$

Here, σ is the electrical conductivity, w_{lam} is the lamination thickness and δ is the material density. This gives what is known as the classical eddy current losses:

$$p_{e,class} = \frac{\sigma \pi^2 w_{lam}^2 \hat{B}^2 f^2}{6\delta} \tag{4}$$

In [20] a loss separation model called CAL2 was proposed. This is the same equation as proposed by Jordan, only with coefficients varying both with the frequency and flux density:

$$p = K_h(f, \hat{B}) \hat{B}^2 f + K_e(f, \hat{B}) \hat{B}^2 f^2 \tag{5}$$

To include non-sinusoidal waveforms in the loss calculation, a time domain extension of the CAL2 model also proposed in [20] may be used. In this model, the coefficients were set to be dependent on the flux density at the fundamental frequency, simplifying the equations. Here, Equation 6 and Equation 7 may be used to represent the hysteresis and eddy current loss components.

$$p_h = \frac{1}{\pi T} \int_0^T K_h(f_1, \hat{B}) \cdot B(t) \cdot \left| \frac{dB(t)}{dT} \right| dt \tag{6}$$

$$p_e = \frac{1}{2\pi^2 T} \int_0^T K_e(f_1, \hat{B}) \cdot \left| \frac{dB(t)}{dT} \right|^2 dt \tag{7}$$

Where the time integration is performed over an electrical cycle of period T. When modelling the variable coefficients, it was found in [20] that a third order polynomial with respect to $\hat{B}$ was a sufficient compromise between a good fit and the experimental data needed:

$$K_h(\hat{B}) = k_{h0} + k_{h1}\hat{B} + k_{h2}\hat{B}^2 + k_{h3}\hat{B}^3 \tag{8}$$

$$K_e(\hat{B}) = k_{e0} + k_{e1}\hat{B} + k_{e2}\hat{B}^2 + k_{e3}\hat{B}^3 \tag{9}$$

Here, k_{h0-3} and k_{e0-3} are constants that may be determined through a curve fit by inserting these expressions into Equation 5 and using a curve fitting tool to find the best fit relative to the steel loss data. In order to take the frequency dependency of the coefficients into account, several frequencies from the loss data should be used in the fit.

2) Magnet losses: The material used in permanent magnets has high conductivity, which means that they are susceptible to large eddy currents induced by flux density variations. These lead to losses that may be calculated through integrating the current density across the surface of a single magnet through the following equation [23]:

$$P = \frac{2L}{T} p_p \int_0^T \int \int_S \frac{J_m^2}{\sigma_m} \, dS \, dt \tag{10}$$

Here L is the axial length, T is the rotational period time, and p_p is the number of pole pairs. σ_m is the conductivity, and J_m is the current density in the magnets. As the rotational speed is 10 rpm, T is equal to 6 seconds, which would require enormous amounts of data. To reduce the time samples needed, T was reduced to one sixteenth of the rotational period time. This is the rotational time corresponding to one module, and the symmetry in the machine indicates that this should yield the same result.

Eddy current losses in the steel of an electric machine are reduced through laminating the core. This is because these losses are proportional to the square of the lamination thickness, as shown in Equation 4. In the same manner, eddy current losses in the magnets may be reduced significantly through dividing a magnet into segments of reduced thickness in the direction perpendicular to the magnetic field. Tangential and axial segmentation, and a combination of the two has proved beneficial for a reduction of magnet losses [24]. Figure 3 shows an example of tangential segmentation and how eddy currents form here compared with a one pieced magnet.

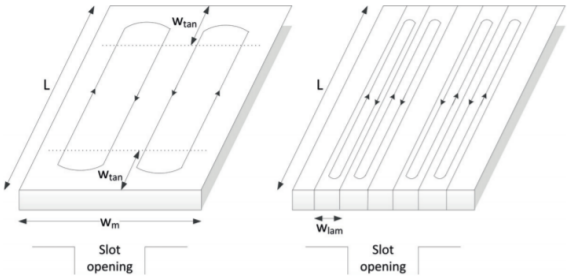

Fig. 3: Eddy current paths in a one pieced magnet and tangentially segmented magnet [25].

The remanent flux density of permanent magnets decreases with an increasing temperature. For temperatures lower than the magnet maximum temperature, this may be approximated through the following equation [26]:

$$B_{r,T} = B_{r,T_0}(1 - \alpha_T(T - T_0)) \tag{11}$$

Where B_r is the remanent flux density, T_0 is defined as 20^oC and T is the magnet temperature. The magnet temperature coefficient, α_T, describes how much the flux density is reduced per degree increased.

3) Copper losses: The copper losses may be found through the following equation [27]:

$$P_{cu} = N_{ph} I^2_{ph,rms}(R_{dc} + R_{skin}(f) + R_{proximity}(f)) \tag{12}$$

Here, N_{ph} is the number of phases and $I_{ph,rms}$ is the RMS value of the phase current. R_{dc}, $R_{skin}(f)$ and $R_{proximity}(f)$ are respectively the DC, skin and proximity components of the phase resistance. At low frequencies, the copper losses are dominated by the Joule effect that is modelled through the DC-resistance [28]. In COMSOL, the DC-resistance of a single homogenized multi-turn coil is defined as follows [29]:

$$R_{dc,coil} = \int_A \frac{NL}{\sigma_{coil} a_{coil} A} dA \tag{13}$$

Where N is the number of turns, L is the axial length and σ_{coil} is the wire conductivity. a_{coil} and A are cross-sectional areas of the wire and entire coil respectively. To get the total resistance for the entire phase, $R_{dc,coil}$ must be multiplied with the number of slots corresponding to it.

C. Radial forces and vibration

1) Space harmonics: In a permanent magnet synchronous machine, the flux in the air gap will not be a pure sine wave in space relative to its position along the rotor periphery. The constant flux density in the permanent magnets gives raise to a square shaped distribution. This is mixed with the MMF from the stator windings. Reluctance variations in the magnetic circuit mainly due to stator slotting leads to a further disturbance of the distribution. The resulting air gap flux contains spatial harmonics that may give raise to unwanted effects such as increased losses or vibrations [30].

Harmonics with a non-zero order lower than the main harmonic are often referred to as *subharmonics*.

2) Radial force density: The radial component of the air gap force density may be calculated through the magnetic field density using the Maxwell stress tensor [31]:

$$f_r = \frac{1}{2\mu_0}(B_r^2 - B_t^2) \tag{14}$$

Where μ_0 is the vacuum permeability, and B_r and B_t are the radial and tangential components of the magnetic flux density in the air gap. In this equation it may be seen that the force density is dependent on the flux density squared. This means that the negative poles of the flux will lead to a positive force, which leads to twice as many poles in the force density than the flux, and a zeroth harmonic corresponding to the average, which is now positive. When doubling the amount of poles, the time it takes until the pattern repeats itself at a given point will halve, and the frequency doubles.

The radial force density in any point along the air gap line may be written as a sum of its harmonics through the Fourier series in the amplitude-phase form [32]:

$$f_r = \sum_m \hat{f}_{rm}(t) cos(2\pi f_m t - m\alpha - \Psi_m) \tag{15}$$

Here, m is the spatial harmonic order, and $\hat{f}_{rm}$ is the peak force density of the harmonic. As time passes, the magnetic field will rotate with the rotor, and the force density at a given point will vary with time. This is modelled through the temporal frequency, f_m. The stationary variation of the harmonic in the spatial domain is included through α, which corresponds to the angular position of any point in the air gap relative to a fixed stator reference. Ψ_m is a spatial phase angle that is unique for each harmonic. The amplitude will vary with time as because of reluctance variations due to slotting [33].

3) Harmonic properties: Harmonic orders of the force density are particularly important to consider when analyzing vibration in a machine. This is because the order corresponds to the number of magnetic poles, which will interact with the stator in their own manner.

The zeroth harmonic corresponds to the average force along the air gap, which will lead to an inward pressure on the entire stator as shown in Figure 4.

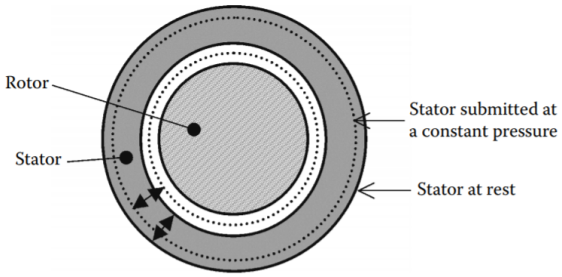

Fig. 4: Stator deformation for m=0 [32].

The harmonic with m=1 will have one point of maximum attraction, stems from a non-centered rotor and will rotate

with the mechanical speed. In this thesis, this is not considered as the rotor is assumed to be perfectly centered.

The force harmonics with $m \geq 2$ will have m points of maximum attraction and will rotate with an angular frequency $\omega_{rot,m}$ as follows:

$$\omega_{rot,m} = \sigma(m)\frac{p}{m}\omega_{mech} \tag{16}$$

The direction of rotation is either clockwise or anti-clockwise and may be different for separate harmonics. This is modelled through $\sigma(m) \in \{-1, 1\}$. This has not been the focus of the thesis and the amplitude of the vibration is assumed to be equal for both directions. Here, p is the pole number and ω_{mech} is the mechanical angular frequency. The force shapes are illustrated in Figure 5 for orders 2 and 4 and in Figure 6 for order 32.

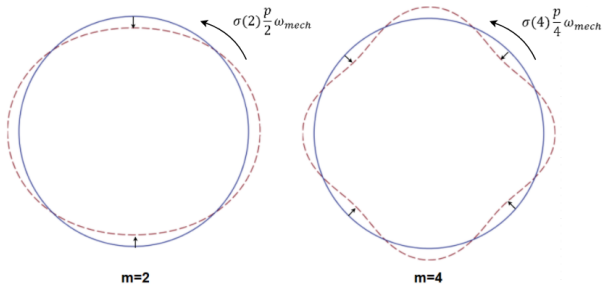

Fig. 5: Stator deformation for m=2 and m=4.

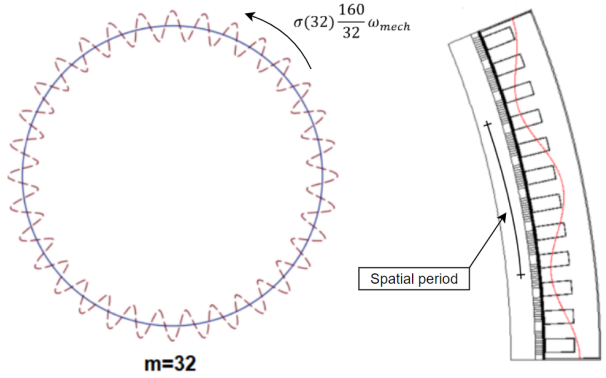

Fig. 6: Stator deformation in entire machine and single module for m=32.

Here, it is clear that each harmonic with $m \geq 2$ corresponds to a stator deformation with 2m poles. The amplitude of the deformation will be dependent on both the force and the mechanical properties of the stator. The spatial period is here defined as the space between each force maximum. The temporal frequency, f_m, corresponds to the time it takes for the harmonic to cover one spatial period. As the pattern repeats itself m times for one mechanical rotation, f_m may be calculated as follows:

$$f_m = m\frac{\omega_{rot,m}}{2\pi} = \frac{p\omega_{mech}}{2\pi} = 2f_{el} \tag{17}$$

The most relevant properties of the radial force density harmonics are listed in Table I.

TABLE I: Properties of radial force density harmonics

Order	$\omega_{rot,m}$	f_m	Effect
m=0	0	0	Uniform attraction between stator and rotor
m=1	ω_{mech}	f_{mech}	One point of maximum attraction
m ≥ 2	$\sigma(m)\frac{p}{m}\omega_{mech}$	$2f_{el}$	m points of maximum attraction

The order of the lowest subharmonic of the radial force density in a permanent magnet synchronous machine is equal to the greatest common divider (GCD) of the number of slots and poles [34], and higher orders will be multiples of this [33].

4) Static deformation: For a standard non-modular stator ring, the amplitude of static deformation of the stator from each harmonic with $m = 0$ and $m \geq 2$ may be expressed through Equation 18 and 19 respectively [32]:

$$Y_{s0} = \frac{RR_y\hat{f}_{rm}}{ET_y} \tag{18}$$

$$Y_{sm} = \frac{12RR_y^3\hat{f}_{rm}}{ET_y^3(m^2-1)^2} \tag{19}$$

Here, R is the internal stator radius, R_y is the average yoke radius, T_y is the yoke radial thickness and E is the Young's modulus of the stator material. The geometric parameters are illustrated in Figure 7.

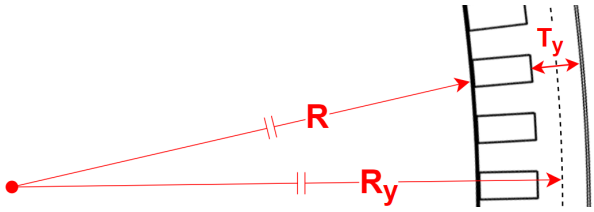

Fig. 7: Geometric parameters for mechanical formulas.

From Equation 19 it is clear that the amplitude of the static deformation for $m \geq 2$ is inversely proportional with m^4, and the lowest harmonics generally have the highest probability of generating vibrations.

5) Eigenfrequencies and resonance: All structures vibrate naturally at certain eigenfrequencies, each having its own mode shape describing the deformation that belongs to it. Both the frequency and the mode shape depends on the mechanical properties and boundary conditions, and may be computed through numerical methods considering all structural details.

Any force harmonic with temporal frequency f_m gives raise to a set of vibrations with the same frequency in an electrical machine. The magnitude of vibration is dependent on the mechanical eigenfrequencies. If the frequency of an exciting force is close to or equal to any of the eigenfrequencies of the stator, it may excite resonance, which could result in dangerous deformations and vibrations [35].

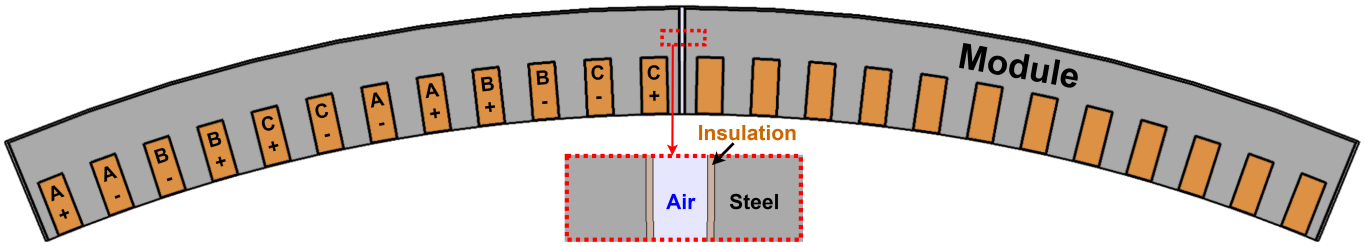

Fig. 8: Implementation of physical modularity and phase layout.

III. MODELLING

The analysis was conducted through 2D finite element modelling in COMSOL multiphysics 5.6. The machine considered was the direct driven permanent magnet generator with 16 modules, 192 slots and 160 magnets, designed for wind power applications in [9]. The design itself was not the focus of the thesis, so only the most relevant properties and modelling decisions are included in this section. Parameters related to the base design, geometry and the electrical system are given Appendix A and C, while material properties are given in Appendix D. To investigate the effect of modularity, a non-modular machine was also modelled. A brief walk-through of the methods used in the analyses, and how they were validated is also presented in this chapter.

A. Assumptions

The following assumptions and simplifications were made in the modelling and analysis:

- While converters of the modular machine are connected in series, the modules of the non-modular machine are connected in parallel. This assumption is made as the insulation requirements of a series connection cannot be met without physical modularity. This will not affect the modelling as the connection is on the converter side.
- Current in coils contains no time harmonics.
- Constant conductivity in all materials.
- Constant temperature of 80 degrees in the permanent magnets.
- End windings and skin and proximity effects were neglected in the calculation of copper losses because of a low frequency.
- Perfectly centered rotor, which makes force harmonic with number 1 equal to zero.
- Rotational direction of force harmonics assumed irrelevant for radial vibration.
- I-beams were only included in eigenfrequency analysis.
- No mechanical interaction between modules because of a large air gap between them.
- Frame is assumed to be infinitely stiff.

B. Model setup

1) Modularity: Modelling of the physical modularity was done through defining an insulation along with an air gap in the tangential ends of the stator module as illustrated in Figure 8.

A non-modular equivalent was made to see the effect of modularity. This model is equal to the modular in all respects other than that the stator is continuous without any air gaps or insulation between modules. As described in the theory about modularity, the converter of each functional module has to be connected in parallel instead of series for the non-modular machine. This does not lead to any changes in the modelling or electrical parameters however, as this connection is on the converter side.

2) Current: In this machine, one base winding has the phase layout presented in Table II.

TABLE II: Phase layout of one base winding

Slot	1	2	3	4	5	6	7	8	9	10	11	12
Phase	A	-A	-B	B	C	-C	-A	A	B	-B	-C	C

There are 12 slots in a base winding, which corresponds to one module as shown in Figure 8. Here, there are two coils per phase in one module. These are coupled in parallel before the converter connection. The current was modelled with a uniform density and was defined as follows for the no load and full load conditions:

TABLE III: Current modelling

Phase	No load	Full load
A	0	$\hat{I}sin(2\pi ft + \theta_q)$
B	0	$\hat{I}sin(2\pi ft + 2\pi/3 + \theta_q)$
C	0	$\hat{I}sin(2\pi ft + 4\pi/3 + \theta_q)$

Here, $\hat{I}$ is the peak slot current, and θ_q is the angle required to align the current with the q-axis. This was found through a time dependent study where the full load current was applied in the coils with a stationary rotor. The time with the maximum torque gives the current angle through the relationship $\theta_q = 2\pi f_e t_{\tau_{max}}$.

3) Mesh: To reduce computation time, the mesh for the general geometry was set to coarse. The maximum element size along the middle air gap boundary marked with blue in Figure 9 was set to 1 mm to get a precise representation of the magnetic field there. In the magnets, the mesh was made extremely fine to get an accurate calculation of the eddy current there. Lastly, a fine mesh was applied for the slot insulation to achieve a converging solution. A section of the mesh in the module edge is illustrated in Figure 9.

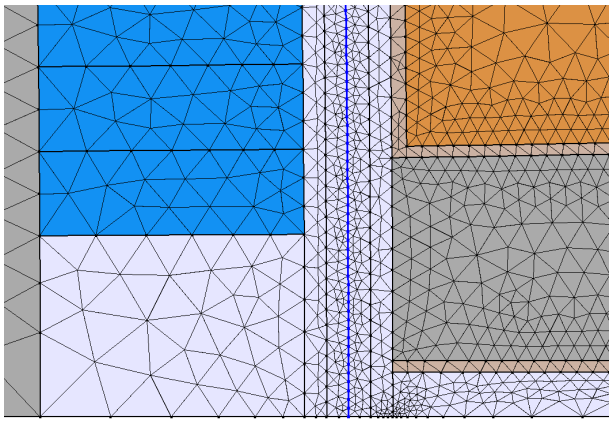

Fig. 9: Mesh in module edge.

4) Tailoring for each analysis: To avoid excessive computation time, it is important to minimize the model with respect to its requirements. The analyses in this thesis had different requirements, and such three separate models were created. To calculate the losses and eigenfrequencies, only simulation of one module was necessary. Boundary conditions and material properties may influence eigenfrequencies significantly. Therefore I-beams were included in this analysis. In the harmonic analysis, half the machine needed to be modelled to get sufficient data for an accurate FFT in MATLAB. This lead to the creation of the models illustrated in Figure 10.

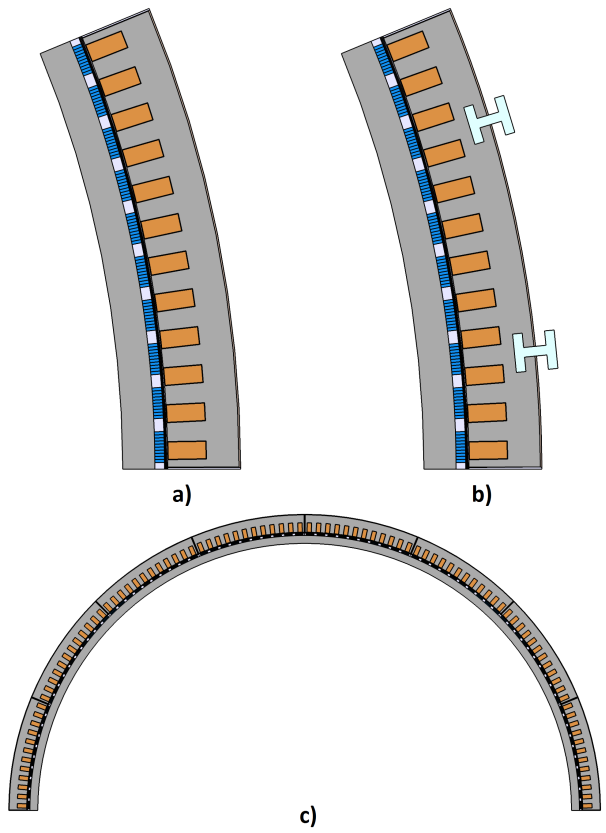

Fig. 10: Model used in analysis regarding a) losses b) eigenfrequencies c) harmonics.

For the models used to calculate losses and harmonics, the *Rotating magnetic machinery* physics were used with a study comprising the *Stationary* and *Time dependent* steps. When calculating module eigenfrequencies, the *Solid mechanics* physics were used in COMSOL's *Eigenfrequency* study.

C. Materials

1) Steel: The steel used both in the stator and rotor was chosen to be non-grain-oriented (NGO) M250-50A because of its low specific power loss. Typical loss data for this material was found in [36] and is given in the appendix. The BH-curve used is shown in Figure 11. This was predefined in COMSOL for NGO 50PN250 silicon steel, and provides values for a field strength up to almost 180 000 A/t.

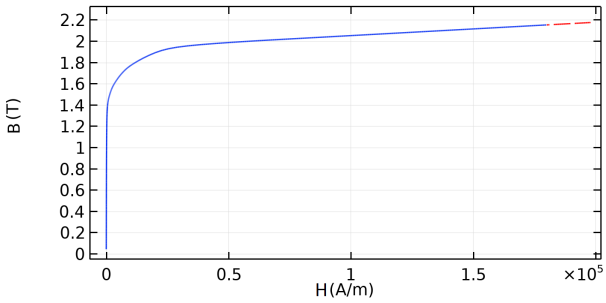

Fig. 11: BH-curve for non-grain-oriented 50PN250 silicon steel [37].

To model laminations in 2D in COMSOL, the conductivity of the steel was set to zero. For the steel, the Young's modulus is different in the rolling and tensile direction because of the manufacturing process. In this thesis, the Young's modulus of the tensile direction is used as this is thought to be in the radial direction.

2) Permanent magnets: NdFeB magnets of grade N45 with an included temperature dependency were assigned for this machine. The temperature in the permanent magnets was assumed to be at the maximum limit of $80°C$. When inserting this into Equation 11 with the given α_T, we find that this reduces the remanent flux density of the magnets with 6% compared to at room temperature.

The initial design was found to have very high magnet losses [38]. To deal with this, tangential segmentation was employed, dividing each magnet into 10 segments of equal size. The number of segments was chosen based on the maximum amount employed in [25]. To model this in COMSOL, each segment was defined as a coil with a net zero current over its cross-sectional area.

3) Coils: The coils consist of concentrated copper windings with 130 turns each. Due to insulation and cavities between the windings, they will have different mechanical properties than a solid block of copper. According to [39], the Young's modulus for the windings can be assumed to be 1/100 of that of a single copper wire. The mass density will also be slightly reduced compared to pure copper because of this. Conductivity was assumed to be constant, not changing with temperature.

4) Insulation: In the eigenfrequency analysis, the insulation of mica had to be specified to include its mechanical properties. For all other analyses, air was used in all insulations as this will have similar magnetic properties.

5) I-beams: To enable the modules to operate at different voltage levels, they must be insulated from the frame. Therefore an insulating material is required in the I-beams. In [40] the use of nylon was proposed. However, E-glass fiber was used in this thesis as it is thought to be more suitable due to it being stiffer and more robust.

D. Analysis methods

1) Losses: Losses in the stator and rotor steel were calculated through implementing the time domain CAL2 equations in the surface integration tool in COMSOL.

The loss coefficients in Equation 8 and Equation 9 were found through the MATLAB curve fitting tool. The typical loss density used as input is given in Figure 24 in the appendix. This only provides data down to 50 Hz, which is significantly higher than the nominal frequency of 13.33 Hz. The frequencies used were 50, 100 and 200 Hz, and all their respective loss data points were utilized. The components of the coefficient polynomials found are given in Table IV.

TABLE IV: CAL2 loss coefficient polynomial constants

Loss coefficient	Value
k_{h0}	0.01525
k_{h1}	0.02271
k_{h2}	-0.03887
k_{h3}	0.01561
k_{e0}	0.0001756
k_{e1}	-0.0001904
k_{e2}	0.0001697
k_{e3}	-4.173e-05

These polynomials are illustrated in the plots shown in Figure 12.

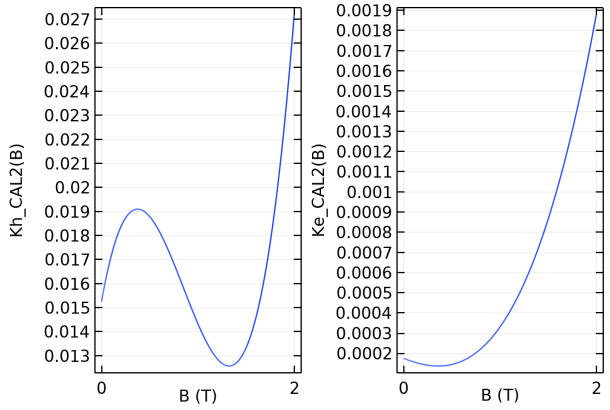

Fig. 12: CAL2 loss coefficients.

The goodness of the fit was evaluated in MATLAB through SSE and R-square. SSE is the sum of squares due to error and measures the total deviation between the fit and the input data. R-square measures how well the variation of the data is included, and a value close to 1 indicates a good fit [41]. These evaluations were found to be very close to ideal as is shown in Table V.

TABLE V: Fit evaluation parameters

Fit parameter	Value	Ideal value
SSE	0.0383 W/kg	0
R-square	0.9999	1

Magnet losses were estimated using Equation 10 in the COMSOL surface integration tool, while the copper losses were found analytically through Equation 12, using the coils dc-resistance obtained through Equation 13. The skin and proximity effects were not included.

2) Harmonic analysis: The harmonic analysis was done through FFT of tables obtained from plots of the radial flux and force densities at a single time instant. MATLAB's discrete FFT-function was used to find the harmonic orders and their amplitude. The script created to do this is shown in Appendix G.

3) Eigenfrequency analysis: For this analysis, I-beams proposed for a modular generator in [40] were implemented. The height of the beams was reduced slightly to better fit the thinner yoke of this machine. They were mounted symmetrically as shown in Figure 13, both just over the B-phase. The frame was assumed to be infinitely stiff to simplify the analysis, and a fixed constraint was set on the outer boundaries of the beams, marked as blue in Figure 13. Other boundaries marked in red were defined as free.

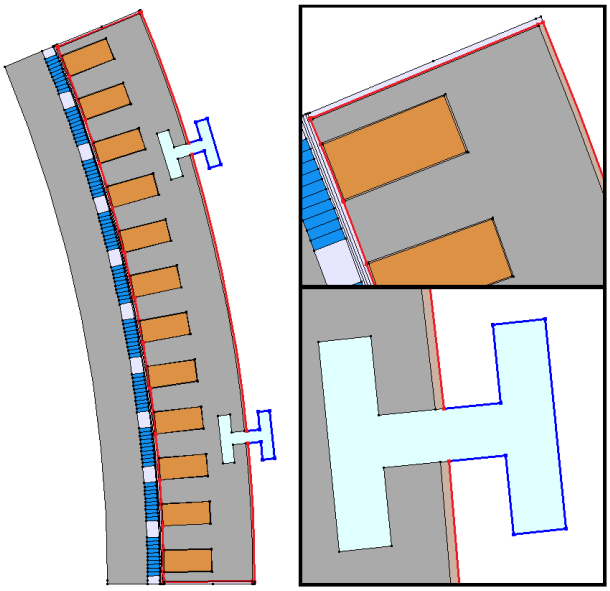

Fig. 13: Model for eigenfrequency analysis with fixed boundary constraints in blue and free boundaries in red.

Here, only the domains for the stator steel, slots, slot insulation and I-beams were included in the physics, as only the eigenfrequencies of a single stator module was considered.

IV. RESULTS

Both losses and forces are very dependent on the electromagnetic performance of the machine. Therefore, this section starts with an overview of the magnetic flux density, before it moves on to losses. The losses are calculated separately, but are summarized in Table X. Then, the orders, amplitudes and frequencies of the force harmonics are presented along with how they are influenced by modularity and time. Static deformation from force harmonics is then calculated before eigenfrequencies of a single module are presented.

For all harmonic analysis, only the harmonics with orders lower than 200 were plotted. This is because subharmonics are generally more likely to cause vibration. Tables containing all flux and force harmonics with amplitudes larger than 0.02 T and 10 kN/m^2 are given in Appendix H.

A. Magnetic flux density

1) Steel flux density: The magnetic flux density at full load is plotted in Figure 14 for the modular and non-modular machine.

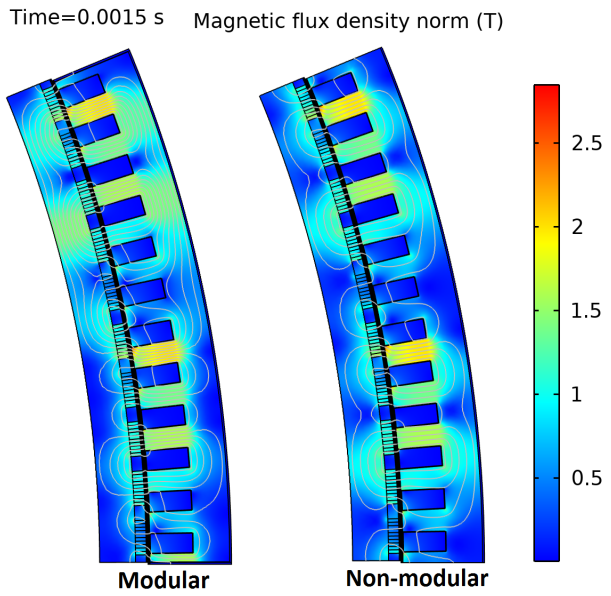

Fig. 14: Full load magnetic flux density at t=1.5 ms.

The flux density was observed to be highest in the extremities of the stator teeth, with maximum values of about 2.8 T. In the middle of the teeth, the peak value was observed to be just below 2 T. The modularity is seen to significantly alter flux paths in the steel. When investigating this further, it was found that the average magnetic flux density for the steel in the modular machine was 0.81 T compared to 0.73 T in the non-modular machine.

2) Air gap flux density: The tangential and radial components of the magnetic flux density in the air gap of one module of the modular machine is given in Figure 15 for both load conditions.

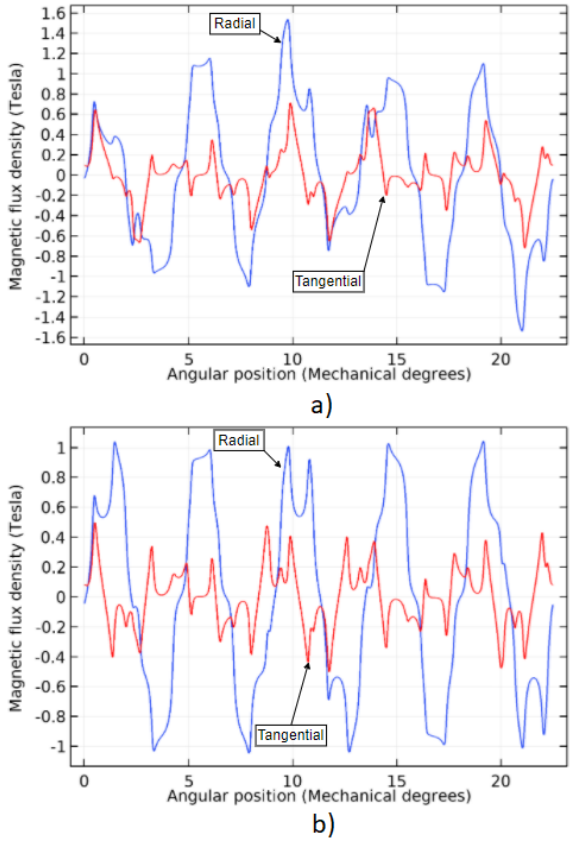

Fig. 15: Spatial distribution of the radial and tangential magnetic flux density in the air gap for one module in modular machine at t=1.5 ms and a) full load b) no load.

This flux pattern was found to repeat for each module. The radial flux density is seen to have a maximum just below 1.6 T at full load and about 1 T at no load. The tangential flux has a peak of about 0.7 T at full load and 0.5 T at no load.

3) Spatial harmonic content: In Figure 16 the spatial harmonic content of the air gap radial flux density in the modular machine is shown.

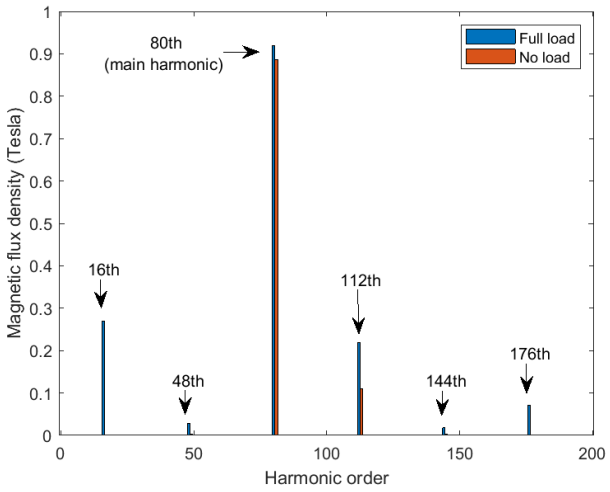

Fig. 16: Spatial harmonic content of radial flux density distribution in air gap of modular machine at t=1.5.

4) Influence of modularity: The influence of modularity on the radial flux density harmonics is shown in Table VI for full load and Table VII for no load.

TABLE VI: Comparison of radial flux density harmonics in air gap of modular and non-modular machine at full load

Harmonic number	Modular [T]	Non-modular [T]	Difference [%]
16	0.270	0.266	1.76
48	0.028	0.033	-13.07
80	0.919	0.917	0.24
112	0.218	0.213	2.36
144	0.018	0.021	-14.46
176	0.070	0.068	2.82

TABLE VII: Comparison of radial flux density harmonics in air gap of modular and non-modular machine at no load

Harmonic number	Modular [T]	Non-modular [T]	Difference [%]
80	0.887	0.888	-0.08
112	0.109	0.109	0.35

For the radial flux density, the 80th harmonic corresponds to the number of pole pairs in the machine and is thus the main harmonic. The difference in this is below 0.25% both at full and no load. At full load, the modularity is found to influence the other harmonics, with a maximum difference in the amplitudes of 0.005 T.

B. Losses

1) Steel losses: The steel losses were estimated both for the full load and no load condition using the CAL2 model in the time domain:

TABLE VIII: Steel losses

Load condition	Loss type	Modular [W]	Non-modular [W]	Difference [%]
Full load	Hysteresis	16 101	13 761	17.0
	Eddy current	8 875	6 703	32.4
	Total	**24 976**	**20 464**	**22.0**
No load	Hysteresis	5 037	3 850	30.8
	Eddy current	1 582	1 182	33.8
	Total	**6 619**	**5 032**	**31.5**

Table VIII shows that the modular machine had 22% higher steel losses than the non-modular at full load, and 31.5% higher at no load. A plot of the steel loss density is given in Figure 17 for full load and in Figure 18 for no load. In the extremities of the teeth edges, the loss density was observed to be up to 150 kW/m^2. However, the color range was manually restricted to 30 kW/m^2 for full load and 10 kW/m^2 for no load to to get a clearer illustration.

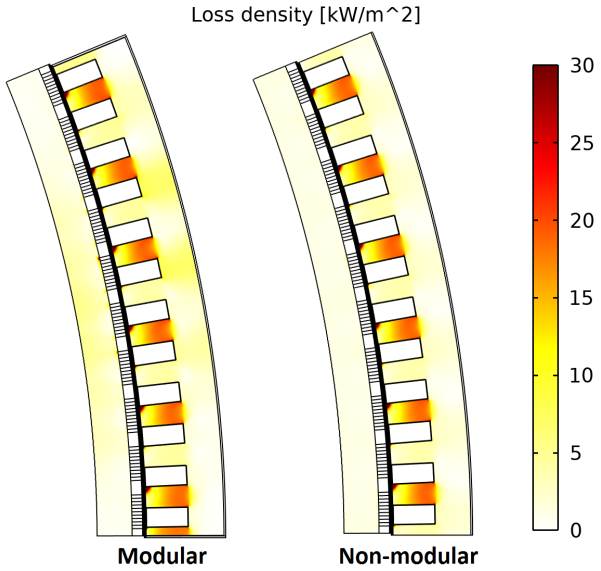

Fig. 17: Loss density in stator and rotor steel at full load.

The loss density at full load is seen to be largest in the teeth, and especially every second tooth, with the highest values at their edges. The increased loss in the modular machine is seen to be distributed across the entire surface, with an additional high loss density in the bottom half tooth.

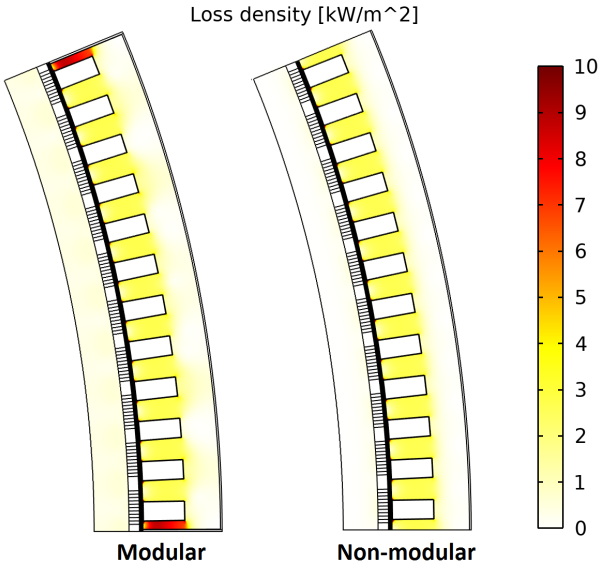

Fig. 18: Loss density in stator and rotor steel at no load.

At no load, the modular machine is seen to have the highest loss density in the half teeth. The losses are also shown to increase slightly across the rest of the steel surface.

2) Magnet losses: Magnet losses were estimated at the full load and no load conditions, both for unsegmented and segmented magnets. The results are given in Table IX.

TABLE IX: Magnet losses

Load condition	Magnet segmentation	Modular [W]	Non-modular [W]	Difference [%]
Full load	Unsegmented	281 090	288 110	-2.4
	Segmented	10 040	10 081	-0.4
No load	Unsegmented	48 663	48 172	1.0
	Segmented	4 351	4 196	3.7

Losses in the modular machine were seen to be reduced at full load and increased at no load. Segmentation reduced the losses with over 96% at full load and 91% at no load. Equation 10 shows that magnet losses are dependent on the square of the current density in the magnets, which is seen to be reduced significantly by the segmentation in Figure 19.

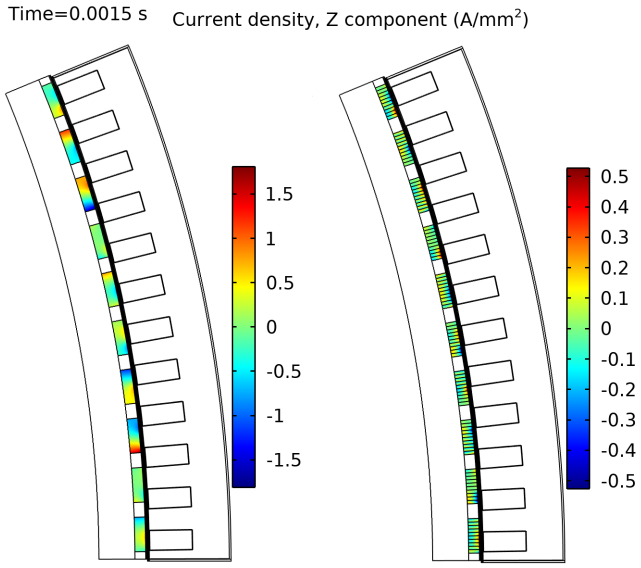

Fig. 19: Current density in unsegmented and segmented magnets at full load.

3) Copper losses: Copper losses were calculated to be 224 740 W at full load. These were equal for the modular and non-modular machine as the current was defined equally.

4) Total losses: The total losses at full load are calculated in Table X.

TABLE X: Total losses at full load

Loss type	Modular [W]	Non-modular [W]	Difference [%]
P_{Steel}	24 976	20 464	22.0
P_{magnet}	10 040	10 081	-0.4
P_{copper}	224 740	224 740	0
Total	**259 756**	**255 285**	**1.8**

Total losses represented approximately 3% of the mechanical power of 8.686 MW found through COMSOL.

C. Radial forces and vibration

1) Air gap force density: In Figure 20, the distribution of radial force density on one module of the modular machine is plotted.

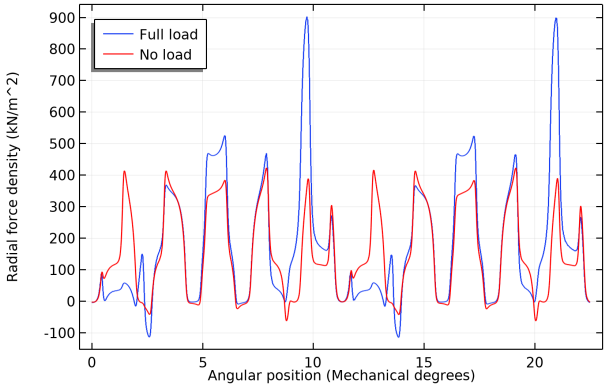

Fig. 20: Spatial distribution of the air gap radial force density for one module at t=1.5 ms.

Here pattern is observed to repeat once over the module. Here, the highest peaks are found to be around 900 kN/m^2 at full load and 400 kNm^2 at no load. At some points, the force density is found to be negative.

2) Spatial harmonic content: The spatial harmonic content of the force density is plotted in Figure 21 for the modular machine at both load conditions.

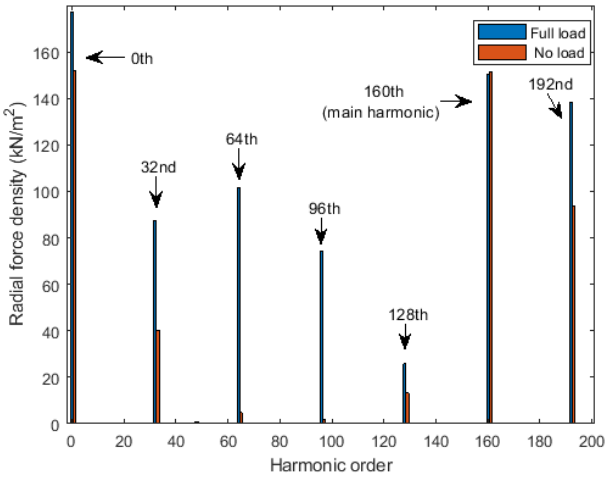

Fig. 21: Spatial harmonic content of radial force density distribution in air gap of modular machine at t=1.5.

The order with highest amplitude is found to be the zeroth, which is the average force density. Other harmonics with high amplitudes are the main harmonic and the 192nd, which corresponds to the number poles and stator slots respectively. At full load, multiple subharmonics are found to be of a considerable size, while at no load they are found to be less prominent.

The greatest common divider between the number of slots and magnet poles is 32, which is observed as the lowest subharmonic present in the machine. All other harmonics are shown to be multiples of 32. The force shapes over one module is presented in Figure 22 for all the subharmonics.

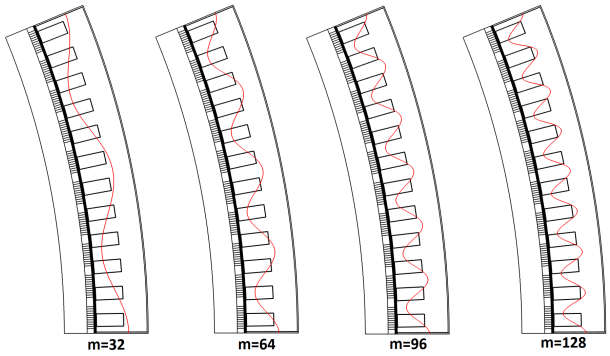

Fig. 22: Force shapes for lower force harmonics.

The temporal frequency for the non-zero harmonics may be calculated through Equation 17:

$$f_m = 2f_{el} = 26.67Hz \tag{20}$$

3) Influence of modularity: The influence of modularity on the spatial harmonic content of the radial force density was investigated at t=1.5 ms. Results for full load and no load are given in Table XI and Table XII respectively.

TABLE XI: Comparison of air gap radial force density harmonics in modular and non-modular machine at full load

Harmonic number	Modular [kN/m^2]	Non-modular [kN/m^2]	Difference [%]
0	177.15	177.59	-0.25
32	87.62	87.45	0.19
64	101.57	102.13	-0.55
96	74.05	74.78	-0.97
128	25.85	25.76	0.36
160	150.55	150.51	0.03
192	138.38	137.95	0.32

TABLE XII: Comparison of air gap radial force density harmonics in modular and non-modular machine at no load

Harmonic number	Modular [kN/m^2]	Non-modular [kN/m^2]	Difference [%]
0	152.07	151.90	0.11
32	40.27	40.51	-0.61
64	4.74	5.17	-8.40
96	1.59	1.85	-14.31
128	13.15	13.28	-0.97
160	151.53	151.01	0.34
192	93.85	93.58	0.29

At full load, the difference between the modular and non-modular machine is shown to be less than 1 % for each harmonic. At no load, the percentage difference is found to be higher for the 64th and 96th. However, these have a very low amplitude, and the difference is less than 0.5 kN/m^2.

4) Time variation of force amplitude: The difference in the spatial harmonic content of the force density for two different time instants of the simulation is shown in Table XIII.

TABLE XIII: Comparison of air gap radial force density harmonics at t=1.5 ms and t=9 ms for modular machine at full load

Harmonic number	t=1.5 ms [kN/m^2]	t=9 ms [kN/m^2]	Difference [%]
0	174.69	168.67	3.57
32	86.41	72.41	19.34
64	97.82	85.14	14.90
96	70.10	62.50	12.16
128	22.83	24.93	-8.41
160	148.74	145.64	2.13
192	135.58	135.93	-0.26

Here, the amplitude of the harmonics is seen to vary with time. As explained in the theory, this is because of reluctance variations and geometric symmetry. After close inspection, this pulsation was also found to have a frequency twice the electrical of 26.67 Hz. The difference is seen to vary between the different harmonics.

5) Static deformation: If the stator ring is assumed to be uniform without the physical modularity, the static deformation may be calculated very simply through Equation 18 and 19. The deformation from the subharmonics found at full load for the non-modular machine was calculated analytically and is given in Table XIV.

TABLE XIV: Static deformation at t=1.5ms assuming uniform stator

Harmonic order	Y_{sm} [mm]
0	0.121
32	$9.34{\cdot}10^{-4}$
64	$6.75{\cdot}10^{-5}$
96	$9.72{\cdot}10^{-6}$
128	$1.07{\cdot}10^{-6}$
160	$2.56{\cdot}10^{-6}$
192	$1.14{\cdot}10^{-6}$

The stator deformation is found to be largest for the zeroth harmonic, while it is decreasing for an increasing harmonic order, as the amplitude is inversely proportional with m^4. The structure in a modular machine is not uniform however, with insulation and air gaps between each module, and the distortion will be very difficult to find analytically. The complexity of the system suggests that an analysis that couples magnetics and mechanics is advised.

6) Module eigenfrequencies: The fifteen lowest module mechanical eigenfrequencies found are listed in Table XV.

TABLE XV: 15 lowest eigenfrequencies of single module

Eigenfrequency [Hz]		
322	1520	2323
362	1609	2344
689	1752	2375
1187	2089	2381
1458	2125	2389

Mode shapes of the five lowest eigenfrequencies are given in Figure 23.

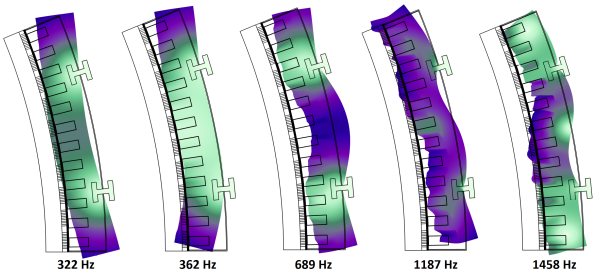

Fig. 23: Mode shapes of lowest eigenfrequencies.

Here, it is clear that the eigenfrequencies of 322 and 362 Hz will have one inward pole per module, and such may be excited by a force harmonic with order 16 as there are 16 modules in the machine. The other mode shapes are more difficult to interpret, but it can be argued that eigenfrequency 1187 has two inward poles, which means it could be excited by the 32nd force harmonic. When examining mode shapes of higher frequencies, given in Appendix J, they were found to be more related to the softness of the windings, and have less influence on the total deformation of the yoke.

V. DISCUSSION

Here, some choices done in the modelling process will first be evaluated, before the results and their validity is analyzed and discussed. When evaluating vibration, force harmonics and mechanical properties are combined as vibration is a result of their interaction.

A. Machine modelling

1) Coil definitions: A series connection of the modules will also require physical modularity as explained in the theory. This means that the non-modular machine has to be connected in parallel, and will not generate the high output voltage that the modular machine will, and the two cases are in that way not entirely comparable. However, these connections will be outside of the machine and will not influence the electrical definitions in COMSOL.

The current was modelled ideally, but in reality it will have time harmonics due to the connection to the converters. Time harmonics could increase losses [30] and further distort the time dependency of the force harmonics. Therefore, an analysis including the effect of time harmonics could be considered.

2) Temperature: The temperature was unknown when modelling and analyzing. In the permanent magnets, the temperature was assumed to be equal to the maximum of $80°C$. This reduced the remanent flux density by approximately 6% compared to room temperature, which will also reduce the steel losses and force density in the air gap as both are dependent on the square of the flux density. Also, the conductivity at $20°C$ was used for all materials. Typically, conductivity decreases with temperature, which would lead to a higher resistance in the magnets and copper coils.

Temperature variations will influence both the performance of the machine as well as the losses and should be investigated more closely to achieve more accurate results. This may be done through a coupled analysis in COMSOL including the *Heat transfer in solids* physics.

3) Support structure: The dimensions of the I-beams were only approximations. To ensure that their design is strong enough to handle all strains, it should be based on an extensive analysis of all forces interacting with a module. Furthermore, the support frame was considered infinitely stiff, and a fixed constraint was set on the outer boundaries of the beams. This approximation could alter the eigenfrequencies, as the frame could also be subject of vibration. However, the complexity of the system due to the modularity quickly becomes difficult to handle, and was considered too advanced for this thesis. The eigenfrequencies obtained here may therefore only be considered as rough estimations.

I-beams were only included in the eigenfrequency analysis. Due to their low permeability, the flux density in the yoke will increase when they are introduced. This may in turn contribute to higher steel losses. An additional concern is that the placement of both the beams adjacent to the B-phase could lead to a worsening of the voltage quality in this phase. These issues could be an interesting area to investigate further. Plots of the magnetic flux density and voltage when including the I-beams are given in Appendix I.

B. Magnetic flux density

In the modular machine, the magnetic flux density in the steel was found to be significantly higher. This could be because the air gaps in the stator structure restrict the flux to flow in less ideal paths. While the modularity did not affect the main harmonic considerably, the difference between other force harmonics in the modular and non-modular machine was found to range between -14.5% and 2.8% at full load. In tesla, the maximum difference is only 0.005 T however, which corresponds to just above 0.5% of the main harmonic.

In the air gap flux density plot, the absolute value of the tangential flux is seen to be generally lower than the radial, and it will therefore contribute less to the radial forces on the stator according to Equation 14. Often it is neglected, but here it was still included as it has considerable peaks of up to 0.7 T.

C. Losses

1) Steel losses: Steel losses were found to be second largest of the losses in the machine, but still accounting for under a tenth of overall losses. The low losses are thought to be mainly because of the machine's unusually low frequency of 13.3 Hz.

In the modular machine, steel losses were found to be 22.0% and 31.5% higher at full load and no load conditions respectively, compared to the non-modular. In the loss density plots, the increased losses are seen to be distributed across the entire steel surface, but with an extra notable increase in the half teeth in the edge of the modules. This could be detrimental to the insulation. However, the magnitude is much lower than the copper losses and should not be the main concern.

A high loss density in every second tooth was found for both the modular and non-modular machine. Additionally, a high density was found both in the bottom half tooth and the middle of the simulated rotor section of the modular machine at full load. Intuitively, losses should have been more equal in all teeth, while rotor losses should be spread more evenly. The cause of this could be the untidy nature of flux in a machine with concentrated windings. High losses in only the bottom half tooth at full load could be because of the direction of the rotation.

To validate the steel loss calculation method, the Bertotti model in the time domain was also employed through the approach described in [38]. The losses using this model were found to be 2.1% higher at full load for the modular machine compared to CAL2. Steel losses are considered difficult to evaluate accurately, and using different loss models could yield a large variation in the results [21]. Therefore this was considered sufficient validation for the steel loss calculation method.

Capabilities of curve fitting routines and loss curve accuracies as well as material manufacturing can add larger inaccuracies than the calculation method [42]. When finding the loss coefficients, frequencies of 50, 100 and 200 Hz were used, while the frequency of the machine was 13.33 Hz. As steel losses increase with the frequency, this most likely lead to an overestimation. The loss data also only provided values up to 1.8 T, and the loss coefficients may not representing losses correctly for flux densities higher than this. With maximum values of the flux density of about 2.8 T, this may be an additional error source. For a more accurate loss approximation, loss data down to 13.33 Hz as well as for higher magnetic flux densities should be requested from the supplier. Also a design factor that accounts for manufacturing should be introduced. This is multiplied with the simulated losses, and in [42], this was found to typically be between 1.4-2.

2) Magnet losses: Through magnet segmentation, the magnet losses were found to decrease by 96% to at full load and 91% at no load. This reduction seemed to be in line with what was found in [25]. The resulting losses were just over 10 kW at full load. While this is the lowest loss component, the magnet losses may still be critical to consider when designing the cooling system. This is because if the magnet temperature increases too much, an irreversible demagnetization could occur [28]. To further decrease the magnet losses, axial segmentation could also be examined.

In this machine, modularization was found to decrease magnet losses slightly at full load, while slightly increasing them at no load. The difference is very small however, and compared to the segmentation, this effect is minimal.

Magnet losses were found both through defining Equation 10 and the built in volumetric loss density function in COMSOL. These functions returned the exact same result, which suggests that COMSOL applies the same equation. In order to validate these losses further, it could be an idea to either calculate them analytically through methods explored in [25] or to measure them on a prototype.

3) Copper losses: Compared to the other losses, the copper losses were very high, and will dominate the heat generation in the machine. Additionally, the steel losses were found to be highest in the teeth. This makes cooling of the stator windings and their closest surroundings a clear focal point in order to avoid degradation of the slot insulation.

In this thesis, the current was defined equally in the modular and non-modular machine. Therefore, the copper losses were also considered equal. However, [9] found that the voltage in the modular machine was 1% lower. This would mean that more current would be required to deliver the same power, which in turn would increase the losses. Furthermore, as much of the steel losses are situated in the teeth, the increase that we saw from modularity could also lead to a slightly higher temperature in the coils. This would lower coil conductivity and such increase losses.

The copper loss calculation was done analytically through Equation 12. Here R_{dc} was both calculated by COMSOL and found analytically through Equation 13, neglecting both end windings and conductivity temperature dependency. R_{skin} and $R_{proximity}$ were neglected as these are less prominent at lower frequencies. All the simplifications made here contribute to a reduction in the losses, and higher losses should be expected. The analytical calculation was validated through the built-in volumetric loss density in COMSOL, which gave equal results.

D. Forces and vibration

In the spatial distribution of the radial force density, peaks of about 900 kN/m^2 were found at full load. Further analysis yielded a zeroth harmonic of almost 180 kN/m^2 at full load, which corresponds to the average force density in the air gap. When designing the support structure, it is important that these strains can be handled as a minimum when considering the magnetic forces. Also weight and other forces should of course be taken into account.

From Equation 19, it is seen that the amplitude of the static deformation is inversely proportional with m^4, and the lowest subharmonic in the force density typically has the highest probability of generating vibrations [34]. In this machine the lowest subharmonic has an order of 32 with an amplitude of 87.6 kN/m^2. While this has a quite large amplitude, the order is very high, and in the non-modular machine, this lead to a static deformation of only $9.34 \cdot 10^{-4}$ mm. According to Equation 19, the vibration would most likely be more critical if the lowest subharmonic had an order of for example 2 or 4. However, air gaps of a modular stator structure will reduce the rigidity of the yoke, which means that the deformation could be more severe in the modular machine.

The temporal frequency of all non-zero harmonics was found to be 26.67 Hz, while the lowest eigenfrequency was estimated to 322 Hz. In order to excite resonances, the temporal frequency must be close to the eigenfrequency. Here, this is far from the case, and the large gap suggests that vibration is unlikely to occur. Furthermore, the mode shape of the two lowest eigenfrequencies corresponded to the force shape of the 16th harmonic, which was not present in this

machine. The eigenfrequency of 1187 Hz had a mode shape that could be excited by the 32nd force harmonic. However, this frequency is 44.5 times higher than the temporal frequencies and is also considered unlikely to be excited.

While there was close to no difference between the radial forces in the modular and non-modular machine, the mechanical properties of the yoke will be very different. Here, this has not been thoroughly investigated. The complexity of the structure suggests that a finite element analysis is needed for further inspection. A coupled analysis in COMSOL including both the *Rotating magnetic machinery* and *Structural mechanics* physics could be the way forward. Here, the forces on each tooth could be modelled through the approach outlined in [33].

In the analysis, only t=1.5 ms was looked at. As was seen in Table XIII, the amplitude of each harmonic varies with time. This time dependency shows that even the zeroth force density harmonic will vary, and such may also cause vibrations. In Table XIII it is shown that this harmonic will cause a much larger static deformation than the others, and a vibration due to this would likely be more severe. However, this time variation was also found to have a frequency of 26.67 Hz, which makes it unlikely to excite any eigenfrequencies of the modules.

In this thesis, tangential vibration has been considered outside of the scope, but should definitely be one of the main focuses going forward. The air gaps between the modules may allow a vibration in the tangential direction that would not be present in a non-modular machine due to the stiff yoke. This is best illustrated by the mode shape of the eigenfrequency of 1187 Hz, which is dragged upwards. Tangential forces and vibration would exert shear stress on the I-beams, which could be very detrimental to the support structure. Frame vibration has also been considered out of scope, but could easily have been included through the approach outlined in [10]. However, the low static deformations found in Table XIV suggest that this will not be an issue.

To validate the approach used in the FFT analysis of flux and force density, the machine with 116 poles and 120 slots from [34], [43], [44] was also modelled in COMSOL. An analysis of the harmonic content of the radial force density was conducted at the no load condition, which yielded the same results as found in [34]. The static deformation and eigenfrequency estimations were not validated.

VI. CONCLUSION

In this thesis, losses and radial vibration in a ModHVDC generator has been presented. A comparison with a non-modular equivalent is included to investigate the effect of the modularity. At full load, total losses in the modular machine were estimated to 259.8 kW, which comprises 3% of the mechanical power. Radial vibration was considered unlikely, and modularity was found to mainly influence steel losses and mechanical properties.

Because of a low electrical frequency of 13.33 Hz, the steel losses only attributed to 25 kW for the modular machine at full load. Modularity increased steel losses by 4.5 kW, or 22% at full load and 1.6 kW, or 31.5% at no load. This resulted in a 1.8% increase in total losses at full load. The additional losses were attributed to a higher flux density in the modular machine, and were found to be distributed across the entire module surface, also adding potential hotspots in half teeth at the module edges.

Originally the machine design had very high magnet losses, amounting to 281 kW at full load. However, magnet segmentation reduced these by 96% to only 10 kW, and was thus considered a necessity for the design. At no load the segmentation reduced magnet losses by 91% from 48.6 to 4.4 kW. The difference in magnet losses between the modular and non-modular machine was found to be between -2.4 and 3.7%. With segmented magnets this difference is considered negligible as it amounts to only 41 W at full load and 155 W at no load.

Copper losses amounted to 224.7 kW at full load, and were such the dominating loss component in this machine. Furthermore, several simplifications were made during copper loss calculations, and higher losses should be expected. The influence of modularity on copper losses was not investigated here, but is thought to increase slightly due potentially lower voltage in modular machine.

The zeroth harmonic of the radial force density was found to be 177 kN/m^2 at full load, and corresponds to the average inward pressure along the air gap. Peaks of around 900 kN/m^2 were found in the spatial distribution. The difference in radial forces from modularity was found to be insignificant, being under 1% for all harmonics at full load.

Even though modularity reduces stator rigidity and the amplitudes of the radial force subharmonics were quite high, radial vibration was considered unlikely. This had two reasons:

- The lowest order of the force subharmonics was 32. Lower orders are considered more likely to cause vibration, and in this context an order of 32 is considered too high to be of concern.
- Force harmonics had temporal frequencies of 26.67 Hz, while the lowest mechanical module eigenfrequency was 322 Hz. The difference between the two is considered far too large to induce resonance.

However, the amplitude of the harmonics was shown to vary with time, which means that the zeroth harmonic also could contribute to vibration. This could be more critical than the 32nd and should be investigated further.

VII. FURTHER WORK

- Coupling *Rotating magnetic machinery* with *Heat transfer in solids* in COMSOL to get an accurate remanent flux density in the magnets and conductivity for all materials. Also this would ensure that the machine is operating at a viable temperature.
- Investigate how modularity affects steel losses at other electrical frequencies.
- Coupling *Rotating magnetic machinery* with *Structural mechanics* in COMSOL to investigate the effects

of magnetic forces closer. A starting point could be through methods discussed in [33].
- Investigate module tangential vibration.
- Finding eigenfrequencies of and radial deformation of frame due to radial forces. This has been done for several other modular machines in [10].
- Include time harmonics from converters in all analyses.
- Conduct electromagnetic analysis while including the I-beams to find how this affects the performance.
- Experiment with different support structures to find how vibration affects them and how this contributes to a module's resonance frequency.

VIII. ACKNOWLEDGEMENTS

I would like to express my gratitude to my supervisors Pål Keim Olsen and Robert Nilssen for providing me with an excellent guidance throughout my fifth year here at NTNU. Startup help with COMSOL from Solveig Strand, along with the help from Mostafa Valavi with providing data on the model used for validation is also deeply appreciated.

REFERENCES

[1] International Energy Agency. Offshore wind outlook 2019.
[2] GWEC. Global wind report 2021.
[3] Pål Keim Olsen. Modular high voltage direct current generator for onshore wind, 2018.
[4] G. Dajaku and D. Gerling. Low costs and high-efficiency electric machines. In *2012 2nd International Electric Drives Production Conference (EDPC)*, pages 1–7, 2012.
[5] G. Dajaku, W. Xie, and D. Gerling. Reduction of low space harmonics for the fractional slot concentrated windings using a novel stator design. *IEEE Transactions on Magnetics*, 50(5):1–12, 2014.
[6] G. Dajaku and D. Gerling. A novel 12-teeth/10-poles pm machine with flux barriers in stator yoke. In *2012 XXth International Conference on Electrical Machines*, pages 36–40, 2012.
[7] Huilin Kang, Libing Zhou, and Jin Wang. Five-phase modular stator surface-mounted permanent magnet machine with reduced space subharmonics. *IEEJ Transactions on Electrical and Electronic Engineering*, 10(S1):S116–S122, 2015.
[8] Marta Karoline Husebø. Segmented stator of a pm machine with concentrated windings, 2019.
[9] Solveig Samseth Strand. Electromagnetic design of modular generators for offshore wind power applications, 2020.
[10] U. Shipurkar, F. Wani, J. Dong, G. Alpogiannis, H. Polinder, P. Bauer, and J. A. Ferreira. Comparison of modular wind turbine generators considering structural aspects. In *IECON 2017 - 43rd Annual Conference of the IEEE Industrial Electronics Society*, pages 3707–3712, 2017.
[11] U. Shipurkar, H. Polinder, and J. A. Ferreira. Modularity in wind türbine generator systems — opportunities and challenges. In *2016 18th European Conference on Power Electronics and Applications (EPE'16 ECCE Europe)*, pages 1–10, 2016.
[12] Bjorn Andresen and Jens Birk. A high power density converter system for the gamesa g10x 4,5 mw wind turbine. In *2007 European Conference on Power Electronics and Applications*, pages 1–8, 2007.
[13] Jens Birk and Bjorn Andresen. Parallel-connected converters for optimizing efficiency, reliability and grid harmonics in a wind turbine. In *2007 European Conference on Power Electronics and Applications*, pages 1–7, 2007.
[14] Chester Ditmanson, Peter Hein, Stefan Kolb, Joaquin Mölck, and Steffen Bernet. A new modular flux-switching permanent magnet drive for large wind turbines. In *2013 IEEE Energy Conversion Congress and Exposition*, pages 896–903, 2013.
[15] Maira Zulqarnain, David Xu, and Bo Yuwen. Multi modular converters with automatic interleaving for synchronous generator based wind energy system. In *Proceedings of The 7th International Power Electronics and Motion Control Conference*, volume 3, pages 2255–2261, 2012.
[16] Maria Stefania Carmeli, Francesco Castelli-Dezza, Gabriele Marchegiani, Marco Mauri, and Daniele Rosati. Design and analysis of a medium voltage dc wind farm with a transformer-less wind turbine generator. In *The XIX International Conference on Electrical Machines - ICEM 2010*, pages 1–6, 2010.
[17] Pål Olsen, Sverre Gjerde, Robert Nilssen, Jorunn Hoelto, and Sverre Hvidsten. A transformerless generator-converter concept making feasible a 100 kv light weight offshore wind turbine: Part i - the generator. pages 247–252, 09 2012.
[18] Sverre S. Gjerde, Paal Keim Olsen, and Tore M. Undeland. A transformerless generator-converter concept making feasible a 100 kv low weight offshore wind turbine part ii - the converter. In *2012 IEEE Energy Conversion Congress and Exposition (ECCE)*, pages 253–260, 2012.
[19] Sverre Skalleberg Gjerde. Analysis and control of a modular series connected converter for a transformerless offshore wind turbine, 2013.
[20] D.M Ionel, M Popescu, M.I McGilp, T.J.E Miller, S.J Dellinger, and R.J Heideman. Computation of core losses in electrical machines using improved models for laminated steel. *IEEE transactions on industry applications*, 43(6):1554–1564, 2007.
[21] Siri Faremo Haukvik. Comparison of iron loss calculation models including rotational loss, 2020.
[22] Andreas Krings. *Iron Losses in Electrical Machines - Influence of Material Properties, Manufacturing Processes, and Inverter Operation*. PhD thesis, KTH, Electrical Energy Conversion, 2014. QC 20140516.
[23] D Ishak, Z.Q Zhu, and D Howe. Eddy-current loss in the rotor magnets of permanent-magnet brushless machines having a fractional number of slots per pole. *IEEE transactions on magnetics*, 41(9):2462–2469, 2005.
[24] Wan-Ying Huang, Adel Bettayeb, Robert Kaczmarek, and Jean-Claude Vannier. Optimization of magnet segmentation for reduction of eddy-current losses in permanent magnet synchronous machine. *IEEE transactions on energy conversion*, 25(2):381–387, 2010.
[25] Astrid Røkke. Permanent magnet generators for marine current tidal turbines, 2017.
[26] David Reigosa, Daniel Fernandez, Maria Martinez, Juan Manuel Guerrero, Alberto B Diez, and Fernando Briz. Magnet temperature estimation in permanent magnet synchronous machines using the high frequency inductance. *IEEE transactions on industry applications*, 55(3):2750–2757, 2019.
[27] Scott D. Sudhoff. Ac conductor losses in power magnetic devices: a multi-objective design approach, 2014.
[28] Yinye Yang, Berker Bilgin, Michael Kasprzak, Shamsuddeen Nalakath, Matthias Preindl, Hossam Sadek, James Cotton, N. Schofield, and Ali Emadi. Thermal management of electric machines. *IET Electrical Systems in Transportation*, 7, 06 2016.
[29] COMSOL. Ac/dc module user's guide, comsol 5.4, 2018.
[30] Xiaodong Liang, Sherif Omar Faried, and Ahmed M. El-Serafi. Space harmonics of synchronous machines calculated by finite-element method. *IEEE Transactions on Industry Applications*, 52(2):1193–1203, 2016.
[31] Z Q Zhu, Z P Xia, L J Wu, and G W Jewell. Analytical modeling and finite-element computation of radial vibration force in fractional-slot permanent-magnet brushless machines. *IEEE transactions on industry applications*, 46(5):1908–1918, 2010.
[32] B. Cassoret, Jean-Philippe Lecointe, and Jean-François Brudny. *Noise and Vibrations of Electrical Rotating Machines*, pages 1–24. 02 2011.
[33] Matthias Boesing. *Acoustic modeling of electrical drives - noise and vibration synthesis based on force response superposition*. 05 2015.
[34] Mostafa Valavi, Arne Nysveen, Robert Nilssen, Robert D. Lorenz, and Terje Rolvag. Influence of pole and slot combinations on magnetic forces and vibration in low-speed pm wind generators. *IEEE Transactions on Magnetics*, 50(5):1–11, 2014.
[35] P.L Timar. Noise and vibration of electrical machines, 1989.
[36] Typical data for sura m250-50a, Cogent Surahammars Bruks AB, Stockholm, Sweden, 2008.
[37] COMSOL. Comsol material library.
[38] Runar Mellerud. Numerical estimation of losses and forces in a pm machine with modular stator, 2020.
[39] Feng Chai, Yi Li, Yulong Pei, and Zongyang Li. Accurate modelling and modal analysis of stator system in permanent magnet synchronous motor with concentrated winding for vibration prediction. *IET Electric Power Applications*, 12(8):1225–1232, 2018.
[40] Magnus Borgersen. Custom design and analysis of modular high voltage dc generator, 2019.

[41] Mathworks. Evaluating goodness of fit, [Online; accessed 4-March-2021].
[42] P. A Hargreaves, B. C Mecrow, and R Hall. Calculation of iron loss in electrical generators using finite-element analysis. *IEEE Transactions on Industry Applications*, 48(5):1460–1466, 2012.
[43] Mostafa Valavi, Arne Nysveen, Robert Nilssen, and Terje Rolvag. Slot harmonic effect on magnetic forces and vibration in low-speed permanent-magnet machine with concentrated windings. *IEEE transactions on industry applications*, 50(5):3304–3313, 2014.
[44] Øystein Krøvel. Design of large permanent magnetized synchronous electric machines: nbsp;low speed, high torque machiines - gererator for diriect driven wind turbine- motor for rim driven thruster, 2011.
[45] Eclipse Magnetics. Ndfeb magnets / neodymium iron boron magnets datasheet, [Online; accessed 14-April-2021].
[46] Shan Gao, Hartmut Kern, Zhen-Min Jin, Till Popp, Shu-Yan Jin, Hong-Fei Zhang, and Ben-Ren Zhang. Poisson's ratio of eclogite: the role of retrogression. *Earth and Planetary Science Letters*, 192(4):523–531, 2001.
[47] NanoAndMore. General description of muscovite mica, [Online; accessed 13-April-2021].
[48] MatWeb. E-glass fiber, generic, [Online; accessed 19-April-2021].
[49] Hui-Zu Shan and Tsu-Wei Chou. Transverse elastic moduli of unidirectional fiber composites with fiber/matrix interfacial debonding. *Composites Science and Technology*, 53(4):383–391, 1995.

IX. APPENDIX

A. Modular direct drive machine model

This machine was built in COMSOL based on the design work done in [9], and investigating that thesis is advised if more parameters and variables are needed. The performance of the machine was estimated through simple calculations in COMSOL.

TABLE XVI: Modular machine model [9]

Symbol	Name	Value	Unit
Base design			
f_e	Electrical frequency	13.33	Hz
n	Speed (counterclockwise)	10	rpm
N_{ph}	# of phases	3	
N_p	# of poles	160	
N_s	# of slots	192	
N_{mod}	# of modules	16	
N_{sec}	# of sections	16	
N_{mseg}	# of magnet segments per magnet	10	
Dimensions			
R_{so}	Outer stator radius	3739	mm
R_{si}	Inner stator radius	3517	mm
R_{ag}	Air gap radius	3507	mm
R_{ro}	Outer rotor radius	3477	mm
R_{ri}	Inner rotor radius	3377	mm
L	Machine length	1500	mm
g	Air gap length	10	mm
l_m	Magnet thickness	30	mm
k_m	Magnet fraction of pole pitch	0.7	
τ_s	Slot pitch	115.1	mm
τ_p	Pole pitch	138.1	mm
h_s	Slot depth	122	mm
w_s	Slot width	56.5	mm
w_t	Tooth width	58.6	mm
T_{slot}	Slot insulation thickness	1.33	mm
T_{earth}	Screen insulation thickness	5	mm
T_{mod}	Module insulation thickness	2.0833	mm
T_{air}	Air gap between modules	10	mm
Electrical parameters at 80° C			
N	# of turns	130	
a_{coil}	Coil wire cross-section area	38.778	mm^2
$\hat{I}$	Peak slot current	164.32	A
θ_q	Current angle	-2.007	rad
E_p	Peak induced voltage	72	kV
P_{el}	Electrical power	8.326	MW
τ_n	Nominal torque	8.294	MN
P_{mech}	Mechanical power	8.686	MW
η	Efficiency	95.9	%

B. Model used for validation of spatial harmonic analysis

This model was used to obtain the results found in [34] using the script for the analysis developed in this thesis. It was built in COMSOL based on mainly an ANSYS-model provided by Mostafa Valavi along with parameters for the same machine found in [44]. It was only simulated at no-load, which makes the electrical parameters superfluous. There was no module or screen insulation in this model.

TABLE XVII: Model used for validation of harmonic analysis [34], [43], [44]

Symbol	Name	Value	Unit
Base design			
f_e	Electrical frequency	50	Hz
n	Speed	51.7	rpm
N_{ph}	# of phases	3	
N_p	# of poles	116	
N_s	# of slots	120	
N_{mod}	# of modules	1	
N_{sec}	# of sections	4	
N_{mseg}	# of magnet segments per magnet	1	
Dimensions			
R_{so}	Outer stator radius	888.5	mm
R_{si}	Inner stator radius	778.5	mm
R_{ag}	Air gap radius	776	mm
R_{ro}	Outer rotor radius	773.5	mm
R_{ri}	Inner rotor radius	725	mm
L	Machine length	55	mm
g	Air gap length	5	mm
l_m	Magnet thickness	22	mm
k_m	Magnet fraction of pole pitch	0.8	
τ_s	Slot pitch	41.0	mm
τ_p	Pole pitch	41.9	mm
h_s	Slot depth	80	mm
w_s	Slot width	22.3	mm
w_t	Tooth width	18.7	mm
T_{slot}	Slot insulation thickness	2.4	mm

C. I-beams for eigenfrequency analysis

TABLE XVIII: Parameters for I-beams used in eigenfrequency analysis [40]

I-beam parameters		
Height	130	mm
Width	120	mm
Web thickness	30	mm
Flange thickness	30	mm
Corner radius	0	mm

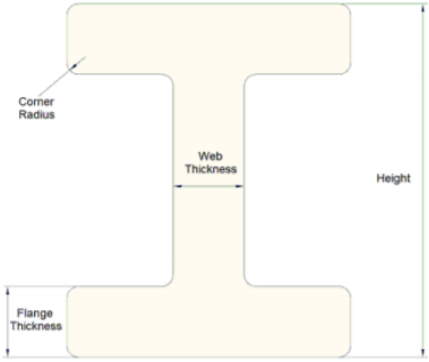

D. Material properties

TABLE XIX: Material properties

Parameter	Value	Unit
Steel (M250-50A) [36], [44]		
Material density	7600	kg/m^3
Iron stacking factor	1	
Lamination thickness	0.5	mm
Young's modulus	190	GPa
Poisson's ratio	0.3	
Copper winding [39], [44]		
Material density	7412	kg/m^3
Conductivity	$5.8 \cdot 10^7$	S/m
Maximum temperature	180	°C
Young's modulus	1.1	GPa
Poisson's ratio	0.35	
NdFeB Magnets [37], [45]		
Grade	N45	
Material density	7500	kg/m^3
Conductivity	713290	S/m
Remanent flux density at 20 °C	1.35	T
Magnet temperature dependency	0.001	
Maximum temperature	80	°C
Relative permeability	1.05	
Air [37]		
Conductivity	0	S/m
Relative permeability	1	
Muscovite mica [37], [46], [47]		
Material density	2900	kg/m^3
Conductivity	$2.01 \cdot 10^{-15}$	S/m
Relative permeability	1	
Young's modulus	170	GPa
Poisson's ratio	0.25	
E-Glass fiber [48], [49]		
Material density	2550	kg/m^3
Conductivity	$2.49 \cdot 10^{-13}$	S/m
Relative permeability	1	
Young's modulus	73.1	GPa
Poisson's ratio	0.22	

Typical data for SURA® M250-50A

T	W/kg at 50 Hz	VA/kg at 50 Hz	A/m at 50 Hz	W/kg at 100 Hz	W/kg at 200 Hz	W/kg at 400 Hz	W/kg at 1000 Hz	W/kg at 2500 Hz
0,1	0,02	0,06	30,6	0,04	0,10	0,28	1,38	5,71
0,2	0,07	0,17	40,7	0,16	0,42	1,15	4,91	19,8
0,3	0,13	0,31	47,9	0,34	0,88	2,41	10,0	41,4
0,4	0,22	0,46	54,5	0,57	1,47	4,03	16,8	71,8
0,5	0,31	0,65	61,3	0,83	2,17	6,03	25,6	113
0,6	0,43	0,86	69,0	1,13	3,00	8,47	36,6	169
0,7	0,55	1,12	77,8	1,47	3,95	11,3	50,3	243
0,8	0,70	1,41	88,6	1,85	5,05	14,7	67,2	338
0,9	0,86	1,77	102	2,28	6,30	18,7	87,8	461
1,0	1,02	2,21	120	2,75	7,73	23,4	113	617
1,1	1,21	2,79	145	3,28	9,36	28,8	143	
1,2	1,42	3,63	186	3,89	11,2	35,2		
1,3	1,67	5,16	278	4,61	13,4	42,4		
1,4	2,02	9,69	584	5,51	15,9	50,9		
1,5	2,38	26,7	1600	6,51	18,9	60,7		
1,6	2,71	68,6	3680					
1,7	2,96	143	6890					
1,8	3,18	263	11600					

Fig. 24: Typical loss density for M250-50A steel [36]

E. Software built-in functions

1) COMSOL: The built-in operators used in COMSOL for modelling and post processing are given in Table XX.

TABLE XX: COMSOL built in functions

Expression	Use
timeint(t1,t2,expr)	Computing integral of expr over given time interval.
d(f,x)	Differentiation of f with respect to x.
timemax(t1,t2,expr,'nointerp')	Find maximum of expr within time period without interpolation.

When computing the time integral outside of the surface integral, the data series operators *Integral* and *Average* found in the COMSOL surface integration tool were used. These calculate the integral and the integral divided by the time interval respectively.

2) Livelink to MATLAB: Table XXI contains the only Livelink functions needed to extract data from COMSOL to MATLAB for post processing.

TABLE XXI: Livelink to MATLAB functions

Expression	Use
Model=mphload('NAME')	Imports COMSOL model to MATLAB
Struct=mphtable(model,'tbl1')	Loads specific table from imported model

Here, 'NAME' is the name defined for the COMSOL mph-file that is loaded. Only one such file may be loaded at a time. When using *mphtable*, the output is a struct with 3 elements. These are column headers, table name and table data. The model's table data may then simply be extracted through the command *Struct.data*.

F. Software definitions

TABLE XXII: Variables defined in COMSOL

Variable	Definition	Description
B_r	(comp1.rmm.Bx*X+comp1.rmm.By*Y)/sqrt(X^2+Y^2)	Radial flux density
B_t	(comp1.rmm.Bx*Y-comp1.rmm.By*X)/sqrt(X^2+Y^2)	Tangential flux density
B_{np}	timemax(0,tmax,rmm.normB,'nointerp')	Peak flux density

TABLE XXIII: Analytic functions defined in COMSOL

Variable	Definition
$K_{h,CAL2}$	$k_{h0} + k_{h1} * B + k_{h2} * B^2 + k_{h3} * B^3$
$K_{e,CAL2}$	$k_{e0} + k_{e1} * B + k_{e2} * B^2 + k_{e3} * B^3$

TABLE XXIV: Surface integrals defined in COMSOL

Description	Definition
$P_{h,CAL2}$	$K_{h,CAL2}(B_{n_p}) * f * (1/pi) * timeint(0, tmax, rmm.normB * abs(d(rmm.normB, TIME))) * L * rho_s * N_{sec}$
$P_{e,CAL2}$	$K_{e,CAL2}(B_{n_p}) * (1/(2 * pi^2)) * f * timeint(0, tmax, abs(d(rmm.normB, TIME))^2) * L * rho_s * N_{sec}$
$P_{e,Bertotti}$	$K_{e,B} * (1/(2 * pi^2)) * (f) * timeint(0, tmax, abs(d(rmm.normB, TIME))^2) * L * rho_s * N_{sec}$
$P_{a,Bertotti}$	$K_{a,B} * (1/(8.76)) * f * (timeint(0, tmax, (abs(d(rmm.normB, TIME)))^{1.5})) * L * rho_s * N_{sec}$
$P_{h,Bertotti}$	$(K_{h,B} * f * B_{n_p}^{\alpha}) * L * rho_s * N_{sec}$
P_{mag}	Avg$(80 * 2 * L * 1/(1/1.4[uohm * m]) * (rmm.JZ)^2)$
P_{Cu}	$16 * L * f * timeint(0, tmax, rmm.Qrh)$

Each surface integral need to be specified over a surface. The steel losses was integrated over both the rotor and stator steel of one module. Magnet losses were integrated over a single magnet (with all its segments), while copper losses were integrated over all the coil domains in a module.

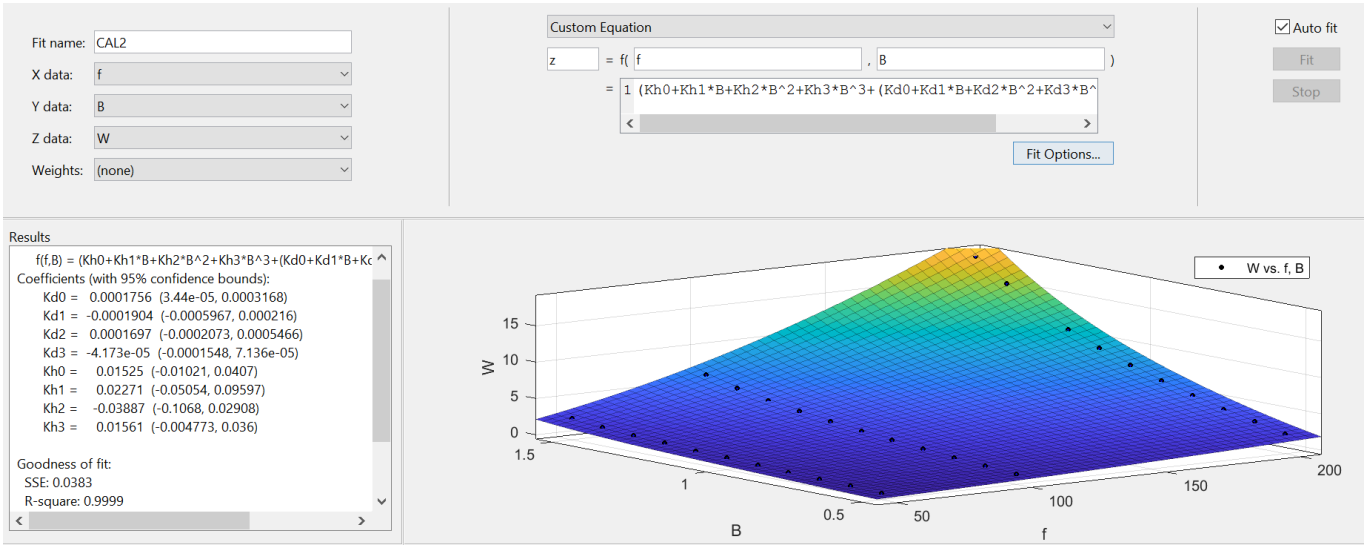

Fig. 25: Curve fit of coefficients for CAL2 model

G. MATLAB scripts

1) FFT script: This script uses a model found through *mphload* as an input and returns a Table with the harmonics of a signal stored in a COMSOL table. The COMSOL table data is assumed to have arc length along the x-axis. The table number in the *mphtable* function should be altered to equal the table number in the COMSOL model.

```
function Table=FFT(model)
Struct=mphtable(model,'tbl1');
ModelTable=Struct.data;
ArcLengths=zeros(1,1);
Times=zeros(1,1);
B=zeros(1,1);
rpm=10;                              %[r/min]
R_ag=3.512;                          %[m]
Circumference=2*pi*R_ag;             %[m]
AGspeed=rpm*Circumference/60;        %[m/s]

%% Transforming from space to time
    domain
for i=1:length(ModelTable)
    ArcLengths(i)=ModelTable(i,1);
    Times(i)=ArcLengths(i)/AGspeed;
    B(i)=ModelTable(i,2);
end
T = Times(2);    %Sampling period
Fs = 1/T;        %Sampling frequency
L=length(Times);
Y=fft(B);
%Returns two sided fast fourier
    transform of B

%% Symmetric two-sided to one-sided
    frequency
%Y-axis:
P2 = abs(Y/L);
P1 = P2(1:L/2+1);
P1(2:end-1) = 2*P1(2:end-1);
%X-axis:
f = Fs*(0:(L/2))/L;
Harmonic_order=f.*(60/rpm);

%% Rounding to integers along x-axis
Table=zeros(1,1);
j=1;
for i=1:length(f)
    if mod(round(Harmonic_order(i)*10)
        /10,1)==0
        Table(j,1)=round(Harmonic_order(
            i));
        Table(j,2)=P1(i);
        j=j+1;
    end
end
end
```

2) Force density bar plots: The bar plots of the radial force density harmonics at both load conditions was found were plotted using the script below. Inputs of the script are the tables that are obtained as the output of FFT.m. When plotting the magnetic flux density, the same script may be used, only altering labels and ticks.

```
function BarplotF(Full_load,No_load)
Table=Full_load(1:100,2);
Table(:,2)=No_load(1:100,2);
x=0:2:199;
x=flip(x);
x=rot90(x);
xd=(x(2)-x(1))/2;
figure(1)
bar(x,Table(:,1),'barwidth',0.5)
hold on
bar(x+xd,Table(:,2),'barwidth',0.5)
xlabel('Harmonic order')
ylabel('Radial force density (kN/m^2)')
yticks([0 20000 40000 60000 80000 100000
    120000 140000 160000])
yticklabels({0, 20, 40, 60, 80, 100,
    120, 140, 160})
end
```

3) Comparison tables: The tables with force density comparison for modes with amplitude over 10 kN/m^2, given in Appendix A were found through the following script. The inputs of the script are the tables that are obtained as the output of FFT.m. Harmonic tables for the magnetic flux density may be found similarly, only through small alterations.

```
function Table=Harmonics(Modular,
    Nonmodular)
Table=zeros(1,1);
t=1;
for i=1:length(Modular)
    if Modular(i,2)>10000 || Nonmodular(
        i,2)>10000
        Table(t,1)=Modular(i,1);
        Table(t,2)=Modular(i,2)/1000;
        Table(t,3)=Nonmodular(i,2)/1000;
        Table(t,4)=(Modular(i,2)-
            Nonmodular(i,2))*100/
            Nonmodular(i,2);
        t=t+1;
    end
end
```

H. Tables for high order harmonics

TABLE XXV: Comparison of radial flux density harmonics with amplitudes over 0.02 T at full load

Harmonic number	Modular [T]	Non-modular [T]	Difference [%]
16	0,270	0,266	1,76
48	0,028	0,033	-13,07
80	0,919	0,917	0,24
112	0,218	0,213	2,36
144	0,018	0,021	-14,46
176	0,070	0,068	2,82
240	0,042	0,043	-0,95
272	0,139	0,139	0,20
304	0,062	0,062	-0,91
400	0,083	0,082	0,21
464	0,045	0,044	2,24
496	0,033	0,032	2,46
560	0,070	0,069	2,07
656	0,030	0,030	-1,28
688	0,022	0,023	-2,29

TABLE XXVI: Comparison of radial flux density harmonics with amplitudes over 0.02 T at no load

Harmonic number	Modular [T]	Non-modular [T]	Difference [%]
80	0,887	0,888	-0,08
112	0,109	0,109	0,35
240	0,040	0,040	-1,36
272	0,143	0,143	0,56
304	0,067	0,067	0,23
400	0,073	0,073	0,11
464	0,040	0,039	3,14
560	0,056	0,056	0,11
656	0,033	0,033	0,34
688	0,026	0,026	1,54

TABLE XXVII: Comparison of radial force density harmonics with amplitudes over 10 kN/m^2 at full load

Harmonic number	Modular [kN/m^2]	Non-modular [kN/m^2]	Difference [%]
0	177.15	177.59	-0.25
32	87.62	87.45	0.19
64	101.57	102.13	-0.55
96	74.05	74.78	-0.97
128	25.85	25.76	0.36
160	150.55	150.51	0.03
192	138.38	137.95	0.32
224	27.43	27.45	-0.10
256	35.25	35.16	0.24
288	31.94	31.74	0.64
320	47.34	47.44	-0.22
352	37.12	36.89	0.60
384	57.86	57.51	0.61
416	22.42	22.35	0.34
480	27.04	26.96	0.28
512	11.09	11.06	0.24
576	45.11	44.97	0.32
640	27.11	27.01	0.36
768	17.50	17.49	0.07
960	16.44	16.24	1.25

TABLE XXVIII: Comparison of radial force density harmonics with amplitudes over 10 kN/m^2 at no load

Harmonic number	Modular [kN/m^2]	Non-modular [kN/m^2]	Difference [%]
0	152.07	151.90	0.11
32	40.27	40.51	-0.61
128	13.15	13.28	-0.97
160	151.53	151.01	0.34
192	93.85	93.58	0.29
224	23.44	23.09	1.50
320	38.92	39.29	-0.95
352	36.52	36.01	1.42
384	25.15	23.77	5.79
416	12.60	13.36	-5.64
480	12.03	11.92	0.92
576	30.78	30.81	-0.07
608	11.16	11.09	0.59
640	19.64	20.01	-1.86
736	12.74	12.15	4.83
768	11.83	10.52	12.45
800	10.43	12.08	-13.65
960	14.56	14.84	-1.95

TABLE XXIX: Comparison of radial force density harmonics with amplitudes over 10 kN/m^2 for t=1.5 ms and t=9 ms for modular machine at full load

Harmonic number	t=1.5 ms [kN/m^2]	t=9 ms [kN/m^2]	Difference [%]
0	174.69	168.67	3.57
32	86.41	72.41	19.34
64	97.82	85.14	14.90
96	70.10	62.50	12.16
128	22.83	24.93	-8.41
160	148.74	145.64	2.13
192	135.58	135.93	-0.26
224	25.23	32.17	-21.58
256	34.01	30.07	13.09
288	30.11	29.36	2.57
320	45.32	25.33	78.91
352	35.28	38.62	-8.64
384	55.08	37.00	48.88
416	20.21	23.75	-14.90
480	25.02	18.43	35.77
512	10.79	2.80	285.61
544	8.48	11.41	-25.68
576	43.52	35.07	24.08
608	7.14	13.15	-45.67
640	26.45	10.91	142.33
736	8.34	12.80	-34.86
768	15.97	16.87	-5.31
800	5.92	14.70	-59.76
960	15.61	16.71	-6.53

I. Performance including I-beams

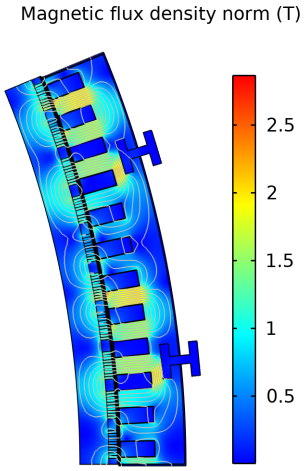

Fig. 28: Magnetic flux density norm in module with I-beams.

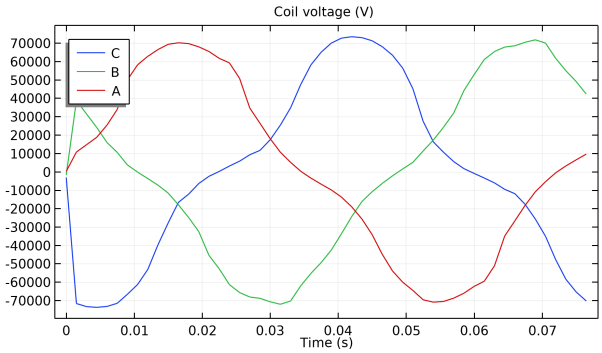

Fig. 29: Voltage in modular machine with I-beams.

J. Mode shapes

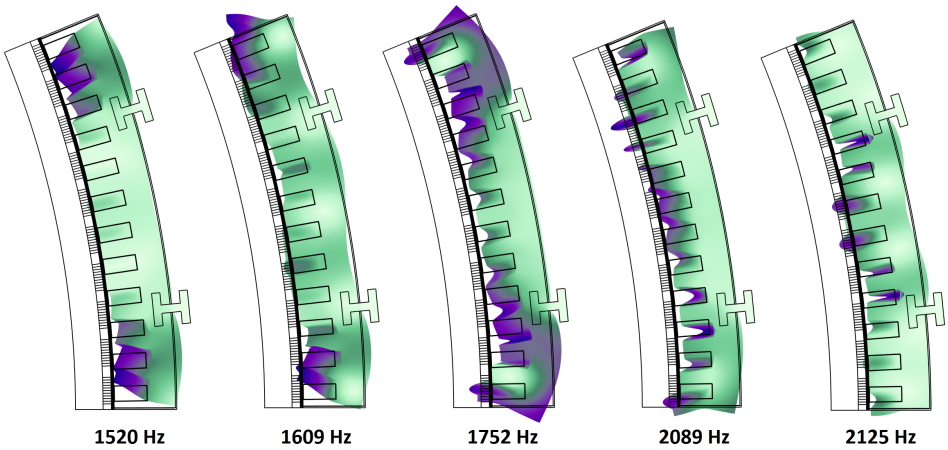

Fig. 26: Mode shapes of eigenfrequency 1520-2125 Hz.

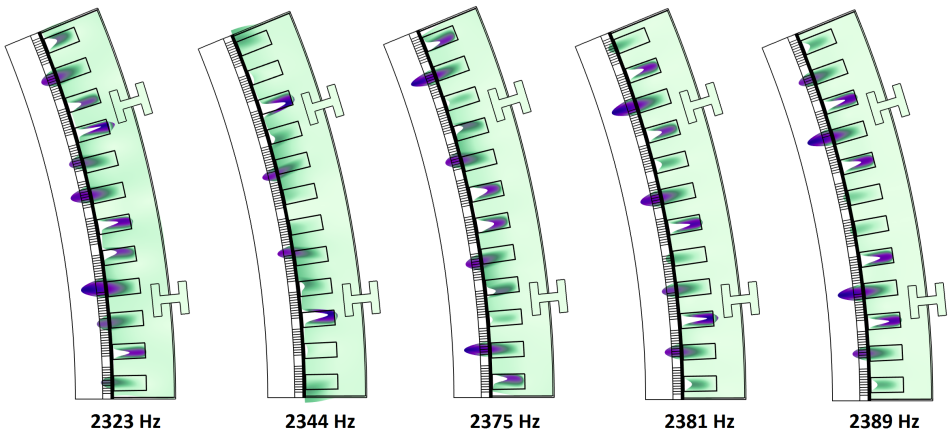

Fig. 27: Mode shapes of eigenfrequency 2323-2389 Hz.

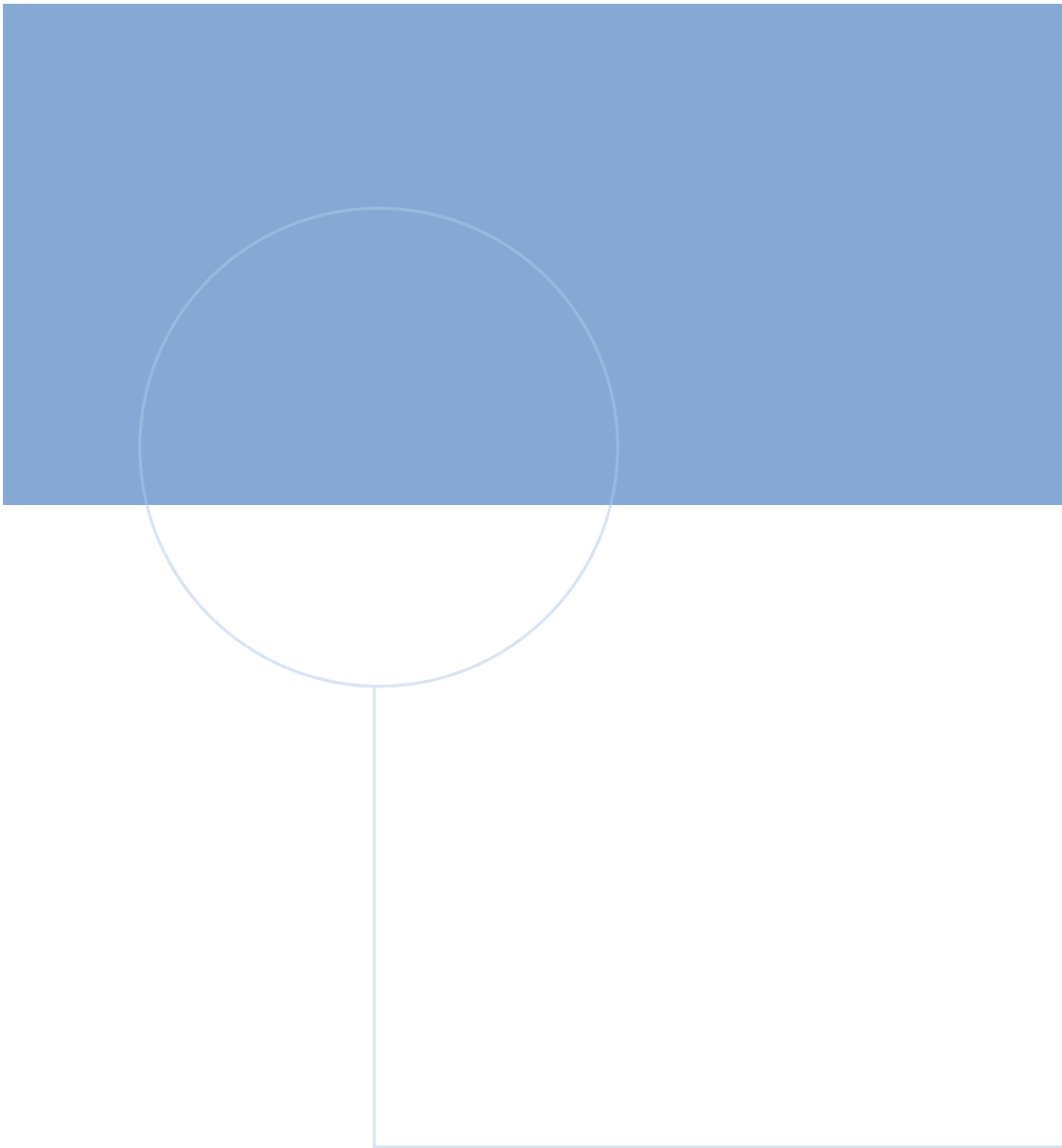

NTNU

Norwegian University of
Science and Technology